

000 001 002 003 004 005 GLOBAL CONTEXT-AWARE REPRESENTATION LEARN- 006 ING FOR SPATIALLY RESOLVED TRANSCRIPTOMICS 007 008 009

010 **Anonymous authors**
 011 Paper under double-blind review
 012
 013
 014
 015
 016
 017
 018
 019
 020
 021
 022
 023
 024
 025
 026

ABSTRACT

027 Spatially Resolved Transcriptomics (SRT) is a cutting-edge technique that cap-
 028 tures the spatial context of cells within tissues, enabling the study of complex
 029 biological networks. Recently, graph-based deep learning has been utilized in
 030 identifying meaningful spatial domains by leveraging both gene expression and
 031 spatial information. However, these approaches fall short in obtaining qual-
 032 ified spot representations, particularly for those located around the boundary of
 033 **spatial domains**, as they heavily emphasize spatially local spots that have min-
 034 imal feature differences from an anchor node. To address this limitation, we
 035 propose a novel framework, **Spotscape**, which introduces the Similarity Tele-
 036 scope module designed to learn spot representations by capturing the global re-
 037 lationships among multiple spots. Additionally, to address the challenges that
 038 arise when integrating multiple slices from heterogeneous sources, we propose
 039 a similarity scaling strategy that explicitly regulates the distances between intra-
 040 and inter-slice spots to ensure they remain nearly the same. Extensive experi-
 041 ments demonstrate the superiority of **Spotscape** in various downstream tasks,
 042 including spatial domain identification, multi-slice integration, and alignment
 043 tasks, compared to baseline methods. Our code is available at the following
 044 link: <https://anonymous.4open.science/r/Spotscape-E312/>

1 INTRODUCTION

045 Recently, Spatially Resolved Transcriptomics (SRT) has gained significant attention for its ability
 046 to capture the spatial context of cells within tissues. Specifically, advanced SRT technologies such
 047 as 10x Visium (Maynard et al., 2021), 10x Xenium (Janesick et al., 2023), seqFISH (Lubeck et al.,
 048 2014), and Stereo-seq (Chen et al., 2022a) provide spatially resolved gene expression data. These
 049 datasets not only contain gene expression profiles, which quantify the activity levels of thousands
 050 of genes within each spot of tissue, but also include spatial coordinates, which represent the exact
 051 physical location of each spot within the tissue. Since much of SRT data analysis focuses on specific
 052 spatial regions or their interactions, spatial domain identification (SDI) serves as a crucial initial
 053 step for categorizing distinct, biologically meaningful tissue regions. For this reason, initial studies
 054 typically employ unsupervised clustering methods (Blondel et al., 2008; Wolf et al., 2018b; Hao
 055 et al., 2021) to group spots based on their original gene expression data. However, they fall short in
 056 predicting accurate **domain identification** results due to the inherent noise in SRT data, which arises
 057 from the limited resolution of the technology, and the high dimensionality of the data.

058 In response to these challenges, various deep representation learning methods have been proposed
 059 to learn spot representations that capture biologically meaningful content by leveraging both spatial
 060 and gene expression data. Specifically, graph-based methods such as SEDR (Xu et al., 2024) and
 061 SpaGCN (Hu et al., 2021) construct graphs based on spatial coordinates to gather information from
 062 nearby spots and generate representations using graph neural networks (GNNs). While this approach
 063 effectively incorporates spatial information into latent representations, it has limitations, particularly
 064 for spots located around the boundary of **different spatial domains**. These boundary spots may
 065 receive information from nodes representing different types of spots (i.e., heterophilic nodes), which
 066 can complicate accurate representation learning.

067 To address this limitation, STAGATE (Dong & Zhang, 2022) proposed leveraging graph attention
 068 networks (GAT) (Veličković et al., 2017) to learn similarities between spots without solely depend-
 069 ing on pre-defined edge weights, thereby enhancing the representations of spots at the boundaries of

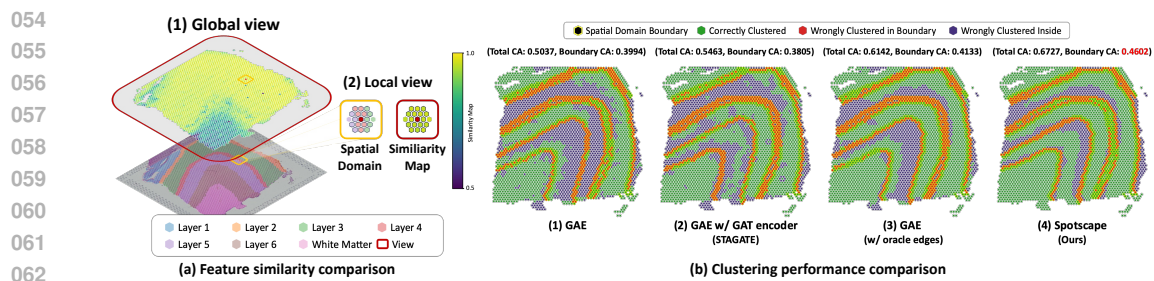


Figure 1: (a) Feature similarity comparison from global and local perspectives. In global view, the similarity between the anchor (i.e., red dot) and other spots gradually changes with their spatial coordinates. In contrast, in the local view, neighboring spots exhibit minimal feature discrepancy compared to the anchor, irrespective of the true spatial domain. (b) Clustering performance comparison in terms of clustering accuracy for all spots (Total CA) and particularly for spots located at the boundary of clusters (Boundary CA) in the human dorsolateral prefrontal cortex (DLPFC) dataset.

spatial domains. Despite the effectiveness of STAGATE, we argue that learning attention weights in the SRT data is particularly challenging due to the *continuous nature* of biological systems, where gene expression values tend to vary smoothly along spatial coordinates (Cembrowski & Menon, 2018; Phillips et al., 2019; Adler et al., 2019; Harris et al., 2021). This inherent continuity can, in some cases, complicate the distinction between different spatial domains (See Figure 1 (a)). Moreover, even if a model successfully assigns appropriate edge weights (e.g., high weights between spots of the same type and low weights otherwise), an anchor spot cannot obtain useful information from its neighboring spots due to the small feature discrepancies between the anchor and its neighboring spots. To corroborate our argument, in Figure 1 (b), we compared clustering performance of various graph autoencoder (GAE) architectures: (1) GAE on the original spatial nearest neighbor (SNN) graph¹, (2) GAE with a GAT encoder, (3) GAE with oracle edge weights², and (4) GAE that incorporates global similarity learning (our proposed method). We observe that while the attention mechanism is helpful for improving the general clustering performance (i.e., Total CA), it rather degrades the clustering performance of boundary spots (i.e., Boundary CA). This highlights the difficulty of learning spot representations near the boundary of **spatial domains** using attention. Another interesting observation is that even with oracle edge weights, improvements in terms of boundary CA is not significant compared with the GAE on the original SNN, supporting our argument that solely relying on the local view provides limited information.

In addition to addressing the aforementioned challenges in the single-slice analysis, representation learning models for the SRT dataset must account for batch effects Li et al. (2020b) to enable multi-slice analysis in the SRT data. Note that the batch effect refers to the phenomenon where spot representations from the same slice are unexpectedly clustered together regardless of their biological relevance, when integrating multiple datasets from different slices. While integrating multiple datasets offers significant advantages, addressing batch effects remains a key challenge.

To this end, we propose a novel framework, **Spotscape**, designed to address challenges in both the single-slice and multi-slice tasks, including Spatial Domain Identification (SDI) (i.e., single-slice task), SRT data integration and alignment (i.e., multi-slice task). To address our findings that exploring only spatially local neighbors yields limited performance gains, **Spotscape** introduces the Similarity Telescope module, which reflects the relative similarity not only among spatially neighboring nodes but also across global spots. More precisely, **Spotscape** generates two augmented views from the SNN graph and minimizes the difference between similarities calculated based on the two augmented views to preserve the meaningful similarities in the global context. This learning scheme is particularly beneficial for SRT data, as optimizing similarity is closely related to the clustering task, which is the most important downstream application. Moreover, **Spotscape** utilizes the prototypical contrastive loss, which groups semantically similar representations together while distancing dissimilar ones, resulting in fine-grained representations. This characteristic is particularly beneficial for addressing challenges that require more detailed representations, such as capturing

¹The SNN graph is constructed by connecting spots that are either within a predefined radius r or among the nearest top k neighbors based on spatial distance.

²Edges between spots of the same type were assigned a weight of 1, and 0 otherwise. That is, we remove heterophilic edges.

rare cell types. Furthermore, we extend **Spotscape** to multi-slice tasks by addressing batch effects through a similarity scale matching strategy that explicitly balances the similarity scales of inter- and intra-relationships. This approach enables the effective mixing of representations across different slices, enabling our model applied to both single and multi-slice SRT data.

In summary, our contributions are four-fold:

- We discover that learning similarity between spatially local neighbors is insufficient for learning representations in the SRT data, especially near the boundary of **spatial domains**.
- To address this limitation, we propose a global similarity learning scheme called the **Similarity Telescope** module to capture the relationships between spots in the global context and adopt prototypical contrastive learning scheme, which helps the model to learn fine-grained representations in the SRT data.
- We propose a similarity scale matching strategy to address batch effects that arise when training multiple slices simultaneously, enabling our model to be effectively applied to both single-slice and multi-slice SRT data.
- We conduct extensive experiments in spatial domain identification, slice integration, and slice alignment to validate the superiority of **Spotscape**.

2 RELATED WORK

2.1 SPATIAL DOMAIN IDENTIFICATION

Spatial domain identification (SDI) is crucial for categorizing biologically meaningful tissue regions and advancing understanding of transcriptional structures, spatial heterogeneity, and cell interactions, thereby aiding insights into tissue organization (Maynard et al., 2021), disease progression (Chen et al., 2022b), and targeted therapies (Maynard et al., 2021; Chen et al., 2022b; Arora et al., 2023). To improve upon traditional clustering methods (Blondel et al., 2008; Wolf et al., 2018b; Hao et al., 2021) used in single-cell RNA sequencing, Giotto (Dries et al., 2021) and BayesSpace (Zhao et al., 2021) leverage hidden Markov random fields and Bayesian techniques, respectively, to incorporate spatial data. Recently, graph-based deep learning methods have emerged to jointly use spatial coordinates and gene expression. For instance, SEDR (Xu et al., 2024) employs a graph autoencoder with masking to learn and denoise spatial gene expression, while SpaGCN (Hu et al., 2021) uses graph neural networks (GNNs) and clustering loss (Xie et al., 2016) for integration of spatial information and gene expression. STAGATE (Dong & Zhang, 2022) applies graph attention networks (GAT) (Veličković et al., 2017) to address boundary heterogeneity. Moreover, self-supervised learning has become popular for capturing robust representations without labels; SpaceFlow (Ren et al., 2022) uses Deep Graph Infomax (DGI) (Veličković et al., 2018) with spatial regularization for spatial consistency, and SpaCAE (Hu et al., 2024) utilizes a graph autoencoder with contrastive learning to handle sparse and noisy spatially resolved transcriptomics (SRT) data effectively.

2.2 SLICE INTEGRATION AND ALIGNMENT

Numerous SRT studies collect data from neighboring tissue sections, but inconsistencies in how the slices are dissected and positioned on the array result in misaligned spatial coordinates. As a result, combining data across different slices is a complex yet essential task to extract diverse and valuable insights. To address this, PASTE Zeira et al. (2022) uses an optimal transport approach to align the spots and integrate them into a shared embedding space. Additionally, SRT data is sometimes generated under varying conditions, such as different technology platforms, developmental stages, or sample conditions. We refer to this as the heterogeneous case, which presents an additional challenge: batch effects, where spot representations from the same slice cluster together, irrespective of their biological significance. To overcome this, STAligner Zhou et al. (2023) defines mutual nearest neighbors as positive samples and utilizes the triplet loss to reduce the distance between anchor and positive samples, facilitating the integration of embeddings across different slices. In addition, GraphST (Long et al., 2023) leverages DGI (Veličković et al., 2018) to maximize mutual information of spots from vertical or horizontal integration to correct batch effect. Moreover, SLAT (Xia et al., 2023) employs a graph adversarial training scheme for robustly aligning spatial slices. Our approach addresses both homogeneous and heterogeneous integration and alignment tasks using a simple similarity scale matching strategy.

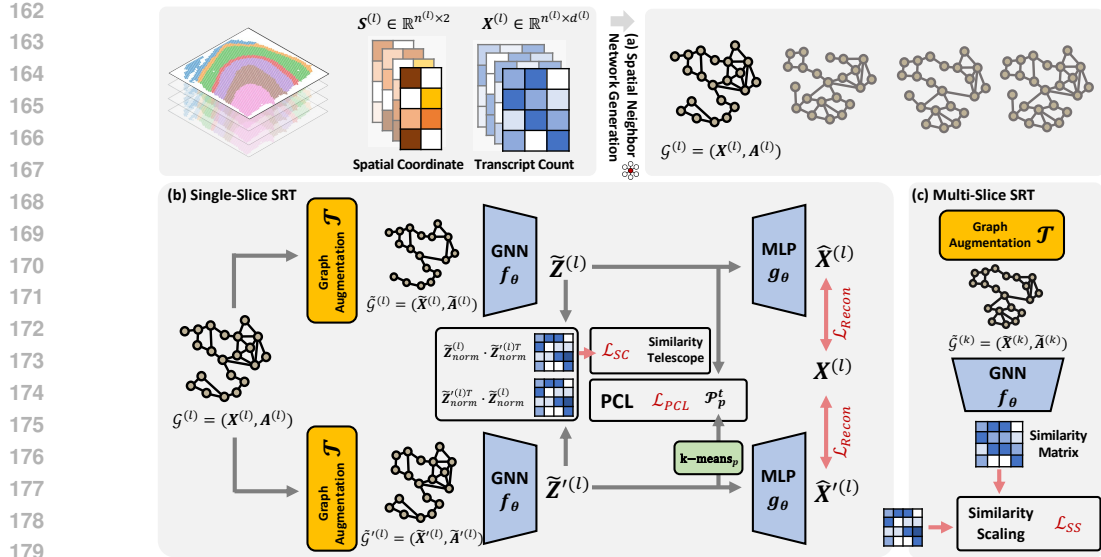


Figure 2: Overall framework of Spotscape. (a) Given SRT data composed of spatial coordinates and transcript counts, we construct a spatial nearest neighbor (SNN) graph. The model is then trained with the SNN graph using (b) similarity telescope and PCL loss, while additionally utilizing (c) similarity scaling loss in multi-slice SRT.

3 PROBLEM STATEMENT

Notations. Given the SRT data composed of spatial coordinates $S \in \mathbb{R}^{N_s \times 2}$ and gene expression profile $X \in \mathbb{R}^{N_s \times N_g}$, where N_s represents number of spots and N_g the number of genes, we construct a spatial nearest neighbors (SNN) graph $\mathcal{G} = (X, A)$ based on distance calculated by spatial coordinates. The adjacency matrix $A \in \mathbb{R}^{N_s \times N_s}$ is defined such that $A_{ij} = 1$ if there is an edge connecting nodes i and j , and $A_{ij} = 0$ otherwise. In multi-slice cases, the spatial coordinates and gene expression profiles are denoted as $S = (S^{(1)}, S^{(2)}, \dots, S^{(N_d)})$ and $X = (X^{(1)}, X^{(2)}, \dots, X^{(N_d)})$, respectively, where N_d represents the number of slices. SNN graphs $\mathcal{G} = (\mathcal{G}^{(1)}, \mathcal{G}^{(2)}, \dots, \mathcal{G}^{(N_d)})$ are computed separately based on their corresponding spatial coordinates.

Task Description. Given the constructed SNN graph \mathcal{G} , our goal is to train a graph neural network (GNN) that generates spot representations without any label information, i.e., self-supervised learning. The trained GNN is then utilized for various downstream tasks, including spatial domain identification (SDI), multi-slice integration, and alignment.

4 METHODOLOGY

In this section, we introduce our method, Spotscape, which is a learning scheme for GNNs applied to the SRT data. In a nutshell, Spotscape learns spot representations by capturing global similarities between spots through the Similarity Telescope module (Sec 4.2), and refining them with cluster assignments using the prototypical contrastive module (Sec 4.3). Furthermore, Spotscape introduces the similarity scaling strategy (Sec 4.4) to balance intra- and inter-slice similarities, thereby alleviating batch effects. The overall framework of Spotscape is depicted in Figure 2.

4.1 MODEL ARCHITECTURE

In this work, we propose novel self-supervised learning strategies specifically tailored for SRT data, while adhering to a basic siamese network structure for our model architecture. In siamese network, we generate two augmented views, $\tilde{\mathcal{G}} = (\tilde{X}, \tilde{A})$ and $\tilde{\mathcal{G}}' = (\tilde{X}', \tilde{A}')$, by applying a stochastic graph augmentation \mathcal{T} to the original graph \mathcal{G} , which consists of node feature masking and edge masking. Then, Spotscape computes spot representations $\tilde{Z} = f_\theta(\tilde{X}, \tilde{A})$ and $\tilde{Z}' = f_\theta(\tilde{X}', \tilde{A}')$, f_θ is a shared GNN-based encoder, $\tilde{Z} \in \mathbb{R}^{N_s \times D}$ and $\tilde{Z}' \in \mathbb{R}^{N_s \times D}$ represent spot representations derived from augmented graph $\tilde{\mathcal{G}}$ and $\tilde{\mathcal{G}}'$, respectively, and D denotes the dimension size of representations.

216 4.2 SIMILARITY TELESCOPE WITH RELATION CONSISTENCY
 217

218 Biological systems exhibit a continuous nature, where gene expression values vary smoothly along
 219 spatial coordinates. This continuity leads to feature similarities between neighboring spots, influenced
 220 both by their spatial proximity and functional characteristics. Therefore, relying solely on
 221 spatially neighboring spots provides limited information, highlighting the importance of reflecting
 222 the global context in this domain. While contrastive learning has become a standard for learning
 223 representations in the global context, it encounters limitations when applied to SRT data. This is
 224 primarily because the characteristics of individual cells cannot be fully defined individually, but
 225 they are influenced by the properties of neighboring cells within the tissue context. To address this,
 226 we propose a novel relation consistency loss for spot representation learning, which aims to cap-
 227 ture the relationship between cells in the biological systems by reflecting the global context among
 228 multiple spots.

229 Specifically, given spot representations \tilde{Z} and \tilde{Z}' , we propose to learn the consistent relationship
 230 that are invariant under augmentation as follows:

$$\mathcal{L}_{\text{SC}}(\tilde{Z}, \tilde{Z}') = \text{MSE}(\tilde{Z}_{\text{norm}} \cdot (\tilde{Z}'_{\text{norm}})^T, \tilde{Z}'_{\text{norm}} \cdot (\tilde{Z}_{\text{norm}})^T) \quad (1)$$

232 where $\tilde{Z}_{\text{norm}} \in \mathbb{R}^{N_s \times D}$ denotes the L2-normalized version of \tilde{Z} , and MSE represents the Mean
 233 Squared Error. That is, we aim to minimize the cosine similarity between the spot representations
 234 that are obtained through differently augmented SNN graph. By doing so, the model learns consis-
 235 tent relationships, which is represented as cosine similarity, between all paired spots under different
 236 augmentations, capturing the continuous variations of spot representations across the entire slice.

237 Additionally, instead of relying on any predictor or stop gradient techniques (Thakoor et al., 2021)
 238 to avoid degenerate solutions, **Spotscape** simplifies the training procedure by employing a recon-
 239 struction loss as follows:

$$\mathcal{L}_{\text{Recon}}(X, \hat{X}, \hat{X}') = \text{MSE}(X, \hat{X}) + \text{MSE}(X, \hat{X}') \quad (2)$$

240 where $\hat{X} = g_\theta(\tilde{Z})$ and $\hat{X}' = g_\theta(\tilde{Z}')$ are reconstructed feature matrices predicted by a shared MLP
 241 decoder g_θ from each augmented view.

242 4.3 PROTOTYPICAL CONTRASTIVE LEARNING
 243

244 While learning spot representations through the similarity telescope module, it is essential for these
 245 representations to be more fine-grained to enable more challenging downstream analyses, such as
 246 identifying rare cell types. To this end, **Spotscape** employs a prototypical contrastive learning
 247 scheme (Li et al., 2020a; De Donno et al., 2023; Lee et al., 2023) that groups semantically similar
 248 representations together while distancing dissimilar ones. Specifically, we obtain prototypes (i.e.,
 249 centroids) by performing K -means clustering on spot representations \tilde{Z}' derived from an augmented
 250 view $\tilde{\mathcal{G}}'$. Pairs of spots assigned to the same prototype are categorized as positive pairs, while pairs
 251 belonging to different prototypes are treated as negative pairs. This clustering process is repeated T
 252 times with varying values of K to identify semantically similar groups across different granularities.
 253 It is formally represented as follows:

$$l_{\text{PCL}}(\tilde{Z}_i, P_{\text{set}}) = \frac{1}{T} \sum_{t=1}^T \log \frac{e^{(\text{sim}(\tilde{Z}_i, p_{\text{map}_t(i)}^t)) / \tau}}{\sum_{j=1}^{K_t} e^{(\text{sim}(\tilde{Z}_i, p_j^t)) / \tau}}, \quad (3)$$

254 where τ represents temperature, and K_t indicates the number of clusters at each level of granularity
 255 during the t -th clustering iteration. $P_{\text{set}} = (P^1, \dots, P^t, \dots, P^T)$ represents the collection of prototype
 256 sets, with each $P^t = (p_1^t, p_2^t, \dots, p_{k_t}^t)$ containing the set of prototype representations for a specific
 257 granularity t . Additionally, $\text{map}_t(\cdot)$ denotes the mapping function that assigns each spot to a corre-
 258 sponding prototype based on the clustering assignments. By applying this to all spot representations,
 259 the overall prototypical contrastive learning (PCL) loss is given as follows:

$$\mathcal{L}_{\text{PCL}} = -\frac{1}{N_s} \sum_{i=1}^{N_s} l_{\text{PCL}}(\tilde{Z}_i, P_{\text{set}}). \quad (4)$$

260 Combining all of these losses, the final training loss for single-slice representation learning is for-
 261 mally defined as:

$$\mathcal{L}_{\text{Single}} = \lambda_{\text{SC}} \cdot \mathcal{L}_{\text{SC}} + \lambda_{\text{Recon}} \cdot \mathcal{L}_{\text{Recon}} + \lambda_{\text{PCL}} \cdot \mathcal{L}_{\text{PCL}} \quad (5)$$

Note to avoid the risk of obtaining inaccurate prototypes, the prototypical loss \mathcal{L}_{PCL} gets involved in the training procedure after a warm-up period (500 epochs) of optimizing only the first two terms in Equation 8.

4.4 SIMILARITY SCALING STRATEGY

Beyond the single-slice SRT, multi-slice SRT allows for the analysis of gene expression patterns across multiple tissue sections. This provides a more comprehensive understanding of the spatial distribution and continuity of gene expression in entire tissues or organs, which could not have been achieved by the single-slice SRT. However, another challenge of learning representations from these multiple slices is the *batch effect*, where spot representations from the same slice are unexpectedly clustered together regardless of their biological significance, hindering researchers from obtaining useful representations related to biological functions. To alleviate this issue, given the SNN graph $\mathcal{G}^{(c)}$ and $\mathcal{G}^{(j)}$ of the current slice c and another slice j , respectively, we explicitly regulate the scale of these similarities to maintain consistency across spots, as described below:

$$\begin{aligned} l_{\text{ss}}(H_i, \mathcal{G}^{(j)}) &= \text{Mean}_{s \in \mathcal{S}_{\text{top}}^{(c)}(H_i[s])} - \text{Mean}_{s \in \mathcal{S}_{\text{top}}^{(j)}(H_i[s])}, \quad \text{for } i \in \mathcal{G}^{(c)} \\ \text{where } \mathcal{S}_{\text{top}}^{(c)} &= \text{Top-}k_{l \in \mathcal{G}^{(c)}}(H_i[l]) = (a_1, a_2, \dots, a_k), \\ \mathcal{S}_{\text{top}}^{(j)} &= \text{Top-}k_{l \in \mathcal{G}^{(j)}}(H_i[l]) = (b_1, b_2, \dots, b_k) \end{aligned} \quad (6)$$

Here, $H = \tilde{Z}_{\text{norm}}(\tilde{Z}'_{\text{norm}})^T \in \mathbb{R}^{N_s \times N_s}$ represents the similarity matrix that we optimize in the Similarity Telescope module, and $H_i[s]$ refers to the element in the i -th row and s -th column of this matrix. The set $\mathcal{S}_{\text{top}}^{(c)}$ includes the top- k most similar spots within the same slice as spot i , and the set $\mathcal{S}_{\text{top}}^{(j)}$ includes the top- k most similar spots in slice j . By doing this, **Spotscape** ensures that the distances between the top- k spots remain nearly the same, regardless of the slice they belong to, effectively mixing all spots from different slices within the latent space. By extending it to all spots and slices, the final similarity scaling loss is given as follows:

$$\mathcal{L}_{\text{SS}} = \frac{1}{N_s(N_d - 1)} \sum_{i=1}^{N_s} \sum_{j=1}^{N_d} \mathbb{1}(i \notin \mathcal{G}^{(j)}) \cdot l_{\text{ss}}(H_i, \mathcal{G}^{(j)}) \quad (7)$$

where $\mathbb{1}(i \notin \mathcal{G}^{(j)})$ is the indicator function that equals 1 if i is not included in $\mathcal{G}^{(j)}$ and 0 otherwise. Finally, the overall loss for multi-slice SRT data is formally represented as:

$$\mathcal{L}_{\text{Multi}} = \lambda_{\text{SC}} \cdot \mathcal{L}_{\text{SC}} + \lambda_{\text{Recon}} \cdot \mathcal{L}_{\text{Recon}} + \lambda_{\text{PCL}} \cdot \mathcal{L}_{\text{PCL}} + \lambda_{\text{SS}} \cdot \mathcal{L}_{\text{SS}} \quad (8)$$

where λ_{SS} is additional balancing parameters of similarity scaling loss.

5 EXPERIMENTS

5.1 EXPERIMENTAL SETUP

Datasets. We conduct a comprehensive evaluation of **Spotscape** across five datasets derived from different technologies. For **single-slice experiments**, we use the dorsolateral prefrontal cortex (**DLPFC**) dataset, which includes 3 patients, each with 4 slices (12 slices in total). Additionally, we assess the middle temporal gyrus (**MTG**) dataset, comprising slices from a control group and an Alzheimer’s disease (**AD**) group, as well as the Mouse embryo dataset. Lastly, we utilize **Non-small cell lung cancer (NSCLC) data**. In **multi-slice experiments**, we integrate the four slices from the same patient in the **DLPFC** dataset for the homogeneous integration task, while analyzing the differences between the control and **AD** groups in the **MTG** dataset for heterogeneous integration. Lastly, we evaluate heterogeneous alignment using the **Mouse embryo** dataset, where slices from different developmental stages require alignment to track developmental progression, and the Breast Cancer dataset, which includes spots corresponding to cancer cell types. Further details about data statistics can be found in Table 8 of Appendix A.

Compared methods. To ensure a fair comparison, we carefully select baseline methods based on their relevance to specific tasks. For the single-slice SDI task, we compare **Spotscape** with five state-of-the arts methods, i.e., SEDR (Xu et al., 2024), STAGATE (Dong & Zhang, 2022),

324

Table 1: Single-slice spatial domain identification performance on DLPFC data.

325

326

DLPFC (Patient 1)																			
Slice 151673					Slice 151674					Slice 151675					Slice 151676				
Silhouette	ARI	NMI	CA		Silhouette	ARI	NMI	CA		Silhouette	ARI	NMI	CA		Silhouette	ARI	NMI	CA	
SEDR	0.24 (0.03)	0.36 (0.08)	0.49 (0.08)	0.55 (0.06)	0.21 (0.04)	0.37 (0.08)	0.48 (0.07)	0.51 (0.07)		0.19 (0.04)	0.33 (0.06)	0.45 (0.06)	0.51 (0.03)		0.21 (0.03)	0.29 (0.03)	0.41 (0.04)	0.47 (0.02)	
STAGATE	0.18 (0.02)	0.37 (0.04)	0.55 (0.03)	0.52 (0.04)	0.17 (0.01)	0.34 (0.03)	0.50 (0.02)	0.51 (0.03)		0.18 (0.06)	0.33 (0.03)	0.5 (0.03)	0.48 (0.03)		0.16 (0.00)	0.33 (0.00)	0.47 (0.01)	0.52 (0.01)	
SpaCAE	0.35 (0.05)	0.21 (0.01)	0.37 (0.01)	0.43 (0.01)	0.27 (0.02)	0.25 (0.03)	0.38 (0.01)	0.44 (0.03)		0.22 (0.02)	0.23 (0.03)	0.41 (0.03)	0.42 (0.04)		0.27 (0.02)	0.23 (0.02)	0.34 (0.02)	0.43 (0.03)	
SpaceFlow	0.43 (0.01)	0.42 (0.06)	0.57 (0.05)	0.57 (0.03)	0.39 (0.05)	0.37 (0.04)	0.51 (0.03)	0.53 (0.03)		0.41 (0.03)	0.38 (0.07)	0.55 (0.06)	0.53 (0.05)		0.41 (0.02)	0.38 (0.05)	0.51 (0.05)	0.53 (0.04)	
GraphST	0.29 (0.01)	0.20 (0.02)	0.34 (0.03)	0.41 (0.02)	0.25 (0.01)	0.27 (0.02)	0.41 (0.01)	0.46 (0.01)		0.31 (0.01)	0.22 (0.02)	0.34 (0.01)	0.40 (0.02)		0.26 (0.01)	0.26 (0.05)	0.40 (0.05)	0.45 (0.04)	
Spotscape	0.46 (0.02)	0.47 (0.03)	0.62 (0.02)	0.62 (0.03)	0.50 (0.02)	0.45 (0.03)	0.58 (0.02)	0.60 (0.01)		0.50 (0.01)	0.46 (0.04)	0.61 (0.02)	0.60 (0.01)		0.49 (0.01)	0.41 (0.04)	0.57 (0.03)	0.55 (0.03)	
DLPFC (Patient 2)																			
Slice 151507					Slice 151508					Slice 151509					Slice 151510				
Silhouette	ARI	NMI	CA		Silhouette	ARI	NMI	CA		Silhouette	ARI	NMI	CA		Silhouette	ARI	NMI	CA	
SEDR	0.10 (0.02)	0.29 (0.06)	0.39 (0.07)	0.45 (0.06)	0.07 (0.02)	0.21 (0.02)	0.31 (0.02)	0.39 (0.02)		0.10 (0.02)	0.37 (0.04)	0.47 (0.04)	0.51 (0.03)		0.08 (0.02)	0.31 (0.05)	0.44 (0.04)	0.47 (0.04)	
STAGATE	0.13 (0.00)	0.41 (0.01)	0.53 (0.01)	0.59 (0.00)	0.14 (0.00)	0.32 (0.01)	0.49 (0.00)	0.54 (0.01)		0.15 (0.01)	0.41 (0.02)	0.57 (0.02)	0.61 (0.04)		0.13 (0.01)	0.32 (0.03)	0.50 (0.02)	0.50 (0.02)	
SpaCAE	0.27 (0.04)	0.28 (0.06)	0.41 (0.06)	0.46 (0.06)	0.29 (0.03)	0.20 (0.04)	0.31 (0.05)	0.40 (0.04)		0.32 (0.01)	0.31 (0.01)	0.44 (0.02)	0.50 (0.04)		0.28 (0.02)	0.27 (0.02)	0.42 (0.03)	0.45 (0.02)	
SpaceFlow	0.39 (0.02)	0.55 (0.03)	0.68 (0.02)	0.71 (0.05)	0.36 (0.03)	0.44 (0.04)	0.57 (0.03)	0.58 (0.04)		0.38 (0.03)	0.53 (0.05)	0.66 (0.02)	0.65 (0.04)		0.37 (0.02)	0.5 (0.03)	0.64 (0.01)	0.61 (0.02)	
GraphST	0.24 (0.01)	0.31 (0.01)	0.45 (0.01)	0.50 (0.01)	0.29 (0.01)	0.34 (0.01)	0.45 (0.02)	0.53 (0.02)		0.26 (0.01)	0.35 (0.01)	0.51 (0.01)	0.55 (0.02)		0.26 (0.01)	0.3 (0.02)	0.47 (0.01)	0.49 (0.03)	
Spotscape	0.46 (0.01)	0.58 (0.05)	0.70 (0.03)	0.73 (0.06)	0.43 (0.02)	0.48 (0.04)	0.63 (0.02)	0.63 (0.03)		0.44 (0.04)	0.55 (0.05)	0.68 (0.03)	0.65 (0.04)		0.43 (0.02)	0.51 (0.03)	0.67 (0.01)	0.61 (0.03)	
DLPFC (Patient 3)																			
Slice 151669					Slice 151670					Slice 151671					Slice 151672				
Silhouette	ARI	NMI	CA		Silhouette	ARI	NMI	CA		Silhouette	ARI	NMI	CA		Silhouette	ARI	NMI	CA	
SEDR	0.16 (0.05)	0.24 (0.07)	0.40 (0.07)	0.48 (0.06)	0.14 (0.02)	0.24 (0.06)	0.39 (0.05)	0.48 (0.05)		0.22 (0.04)	0.37 (0.10)	0.50 (0.09)	0.59 (0.07)		0.21 (0.04)	0.49 (0.09)	0.58 (0.06)	0.66 (0.07)	
STAGATE	0.19 (0.05)	0.29 (0.05)	0.45 (0.07)	0.52 (0.04)	0.14 (0.00)	0.20 (0.01)	0.38 (0.01)	0.44 (0.01)		0.17 (0.02)	0.40 (0.07)	0.49 (0.03)	0.63 (0.06)		0.18 (0.05)	0.38 (0.02)	0.51 (0.04)	0.54 (0.01)	
SpaCAE	0.30 (0.02)	0.21 (0.02)	0.28 (0.03)	0.43 (0.02)	0.27 (0.07)	0.21 (0.01)	0.28 (0.02)	0.43 (0.04)		0.38 (0.16)	0.38 (0.16)	0.29 (0.01)	0.49 (0.05)		0.32 (0.07)	0.25 (0.04)	0.35 (0.05)	0.50 (0.01)	
SpaceFlow	0.44 (0.03)	0.30 (0.07)	0.48 (0.03)	0.51 (0.05)	0.42 (0.03)	0.34 (0.04)	0.50 (0.03)	0.56 (0.05)		0.43 (0.04)	0.54 (0.04)	0.67 (0.02)	0.67 (0.04)		0.46 (0.01)	0.60 (0.06)	0.70 (0.02)	0.73 (0.06)	
GraphST	0.25 (0.01)	0.17 (0.04)	0.26 (0.03)	0.43 (0.02)	0.38 (0.01)	0.14 (0.01)	0.23 (0.00)	0.37 (0.01)		0.28 (0.01)	0.30 (0.01)	0.38 (0.01)	0.54 (0.05)		0.31 (0.02)	0.23 (0.01)	0.32 (0.02)	0.49 (0.01)	
Spotscape	0.54 (0.02)	0.45 (0.02)	0.57 (0.03)	0.65 (0.02)	0.48 (0.01)	0.45 (0.03)	0.55 (0.01)	0.66 (0.02)		0.52 (0.06)	0.59 (0.12)	0.69 (0.05)	0.72 (0.11)		0.56 (0.04)	0.72 (0.05)	0.72 (0.02)	0.82 (0.04)	

340

Table 2: Single-slice spatial domain identifica-
341 tion performance on MTG data.

342

MTG - Control Group				MTG - AD Group				
Silhouette	ARI	NMI	CA	Silhouette	ARI	NMI	CA	
SEDR	0.46 (0.03)	0.41 (0.02)	0.59 (0.02)	0.52 (0.02)	0.32 (0.06)	0.43 (0.08)	0.59 (0.07)	0.57 (0.07)
STAGATE	0.35 (0.01)	0.54 (0.06)	0.65 (0.03)	0.72 (0.01)	0.51 (0.01)	0.58 (0.01)	0.59 (0.01)	
SpaCAE	0.27 (0.01)	0.34 (0.01)	0.44 (0.01)	0.52 (0.01)	0.27 (0.01)	0.34 (0.01)	0.44 (0.01)	0.51 (0.01)
SpaceFlow	0.46 (0.03)	0.66 (0.03)	0.74 (0.03)	0.70 (0.03)	0.40 (0.02)	0.54 (0.03)	0.71 (0.06)	0.65 (0.03)
GraphST	0.49 (0.01)	0.38 (0.01)	0.51 (0.01)	0.48 (0.01)	0.34 (0.02)	0.43 (0.03)	0.55 (0.05)	0.55 (0.04)
Spotscape	0.53 (0.00)	0.73 (0.02)	0.78 (0.00)	0.75 (0.02)	0.48 (0.01)	0.68 (0.02)	0.75 (0.01)	0.77 (0.03)

343

SpaCAE (Hu et al., 2024), SpaceFlow (Ren et al., 2022), and GraphST (Long et al., 2023). For homogeneous integration, we add two more methods, PASTE (Zeira et al., 2022) and STAligner (Zhou et al., 2023), making a total of seven methods. For heterogeneous tasks, we compare with GraphST and STAligner(Zhou et al., 2023), while for heterogeneous alignment, we compare with STAligner and SLAT (Xia et al., 2023), both specialized for alignment tasks. Further details about each method’s adoptable application can be found in table 9 of Appendix B.

344

Evaluation Protocol. Since Spotscape and all other baseline methods focus on learning representations for each spot, we first obtain the representations from each method and then apply the same evaluation tools for the subsequent downstream tasks. For single-slice spatial domain identification, we use K -means clustering on all the obtained representations and evaluate the results using Silhouette score, Adjusted Rand Index (ARI), Normalized Mutual Information (NMI), and Clustering Accuracy (CA). For multi-slice integration, we report the same clustering performance metrics as in the single-slice experiments and additionally include batch correction evaluation metrics such as Silhouette Batch, iLISI, kBET, and Graph Connectivity to assess the effectiveness of batch effect correction. For alignment, we make the alignment using the ‘spatial matching’ function provided by SLAT (Xia et al., 2023) and evaluate the Label Transfer ARI (LTARI), which measures the agreement between the true labels and the labels assigned through the alignment process, providing an evaluation of the alignment quality. **To ensure a fair comparison, we conducted a hyperparameter search for all baseline methods and Spotscape.** Since the optimal hyperparameters for each baseline method may vary across datasets, we identified the best-performing hyperparameters based on the NMI using the first seed. Details of the selected parameters and the corresponding search space are provided in Supplementary Section E All experimental results are averaged over 10 runs with different seeds, and the means and standard deviations are reported for each experiment.

370

5.2 SINGLE-SLICE EXPERIMENTAL RESULTS

371

Experimental results on three different datasets are reported in Table 1, Table 2 and 3, which show the SDI performance on the DLPFC, MTG, and Mouse Embryo datasets, respectively. From these results, we have the following observations: **1) Spotscape** consistently outperforms in all 15 slices across three datasets in terms of Silhouette score, ARI, NMI, CA. We argue that this is because Spotscape not only explores information from spatially local neighbors, which provides limited insights due to the continuous nature of SRT data, but also leverages information within a global

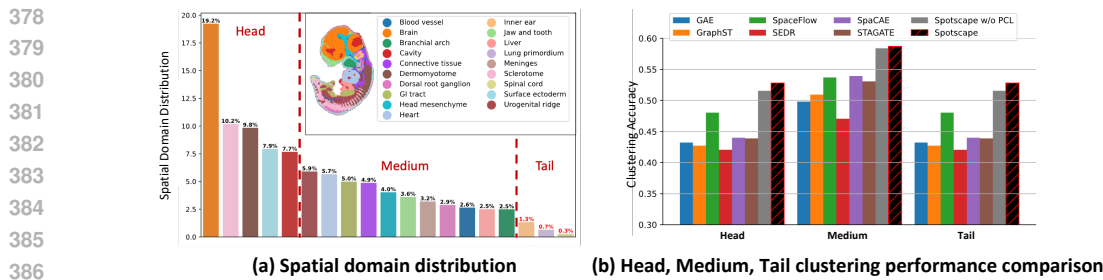


Figure 3: (a) Spatial Domain distribution of Mouse Embryo data and (b) comparison of clustering accuracy across head, medium, and tail types.

context. 2) Although previous methods like SpaceFlow, SpaCAE, and GraphST learn spot representations by incorporating the global context through Deep Infomax or contrastive learning and show generally better results than SEDR and STAGATE both of which only focus on the local view, optimizing similarities proves more beneficial for spatial domain identification, as it is closely related to the relative distance in the latent space. To further clarify this argument, we also conduct additional performance comparison with general self-supervised learning methods in Appendix B. 3) Furthermore, to examine whether Spotscape effectively captures fine-grained information of rare cell types, we conduct a deeper analysis of the Mouse Embryo data, which displays imbalanced spatial domain distributions, as shown in Figure 3 (a). To achieve this, we initially categorize the cells into head, medium, and tail classes based on their distribution. The bottom 3 spatial domains, comprising less than 2%, were classified as the tail, while the top 5 domains showing significant changes in distribution were classified as the head, and the remaining domains were defined as medium, and then assess the performance for each class. As shown in Figure 3 (b), Spotscape outperforms the baselines across head, medium, and tail cell classes, highlighting its capability to capture fine-grained information of cells within rare spatial domains. Furthermore, we observe that model performance declines across all classes when the prototypical contrastive loss (Spotscape w/o PCL) is removed. This indicates that the prototypical contrastive loss enhances the model’s ability to achieve fine-grained cell representation through a multi-granularity clustering approach, thereby contributing to clustering rare cell types.

5.3 MULTI-SLICE EXPERIMENTAL RESULTS

Homogeneous Integration Results. Among the multi-slice experiments, we first start with homogeneous integration tasks, which aim to integrate multiple slices from the homogeneous sample. To do so, we conduct experiments on the DLPFC data used for single-slice experiments, which consists of multiple slices obtained from vertical cuts of a single patient. Since these slices are from a single patient, they do not exhibit significant batch effects, enabling us to incorporate both multi-slice integration methods as well as single-slice SDI methods as baselines. As shown in Table 5, we observe Spotscape consistently outperforms all baseline methods, demonstrating its effectiveness in integrating information from the multiple slices from homogeneous sample.

Heterogeneous Integration Results. For the heterogeneous integration experiments, we assess the model’s ability in integrating two distinct types of samples—the control group and the AD group in the MTG data—to analyze the differences between them. In this experiment, we also report batch effect correction metrics, such as Silhouette Batch, iLISI, kBET, and Graph Connectivity, to evaluate the effectiveness of correcting batch effects, along with clustering metrics. In Table 6, Spotscape demonstrates its effectiveness in integrating multi-slice data in terms of both clustering and batch effect correction, showing significantly better performance than the baselines. Moreover, in Figure 4, we observe that Spotscape’s spot representations from different slices are well integrated while preserving their biological meaning. We also observe that the model performance significantly degrades without similarity scaling module (i.e., Spotscape w/o SS), while this effect is not as pronounced in homogeneous slices (Table 5), where batch effects are negligible. These results indicate the effectiveness of the similarity scaling module in mitigating batch effects when handling multiple slices.

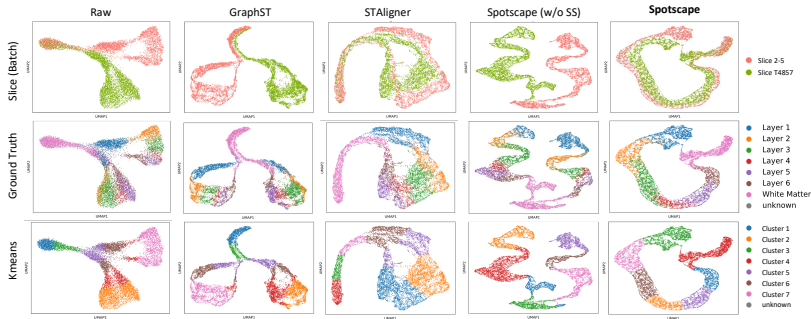
432
433
434
435
436
437
438
439
440
441

Table 5: Homogeneous integration performance on DLPFC data.

	Patient 1				Patient 2				Patient 3			
	Silhouette	ARI	NMI	CA	Silhouette	ARI	NMI	CA	Silhouette	ARI	NMI	CA
SEDR	0.30 (0.02)	0.38 (0.06)	0.49 (0.06)	0.56 (0.06)	0.22 (0.03)	0.32 (0.05)	0.44 (0.07)	0.48 (0.07)	0.31 (0.02)	0.43 (0.02)	0.51 (0.01)	0.56 (0.03)
STAGATE	0.16 (0.03)	0.31 (0.03)	0.46 (0.03)	0.49 (0.03)	0.10 (0.01)	0.30 (0.02)	0.46 (0.01)	0.48 (0.02)	0.14 (0.03)	0.31 (0.09)	0.43 (0.06)	0.54 (0.08)
SpaCAE	0.21 (0.01)	0.21 (0.03)	0.36 (0.02)	0.40 (0.02)	0.13 (0.03)	0.12 (0.06)	0.19 (0.07)	0.32 (0.05)	0.20 (0.05)	0.13 (0.05)	0.14 (0.05)	0.43 (0.06)
SpaceFlow	0.31 (0.01)	0.48 (0.03)	0.60 (0.02)	0.60 (0.02)	0.27 (0.02)	0.44 (0.05)	0.59 (0.02)	0.58 (0.04)	0.30 (0.03)	0.51 (0.02)	0.60 (0.01)	0.69 (0.05)
GraphST	0.30 (0.02)	0.18 (0.01)	0.32 (0.01)	0.38 (0.02)	0.30 (0.01)	0.25 (0.01)	0.39 (0.01)	0.42 (0.02)	0.30 (0.01)	0.25 (0.04)	0.30 (0.04)	0.50 (0.01)
PASTE	0.15 (0.00)	0.34 (0.00)	0.45 (0.00)	0.54 (0.00)	0.11 (0.00)	0.17 (0.00)	0.28 (0.00)	0.40 (0.00)	0.11 (0.00)	0.29 (0.00)	0.43 (0.00)	0.54 (0.00)
STAligner	0.34 (0.04)	0.38 (0.04)	0.52 (0.04)	0.55 (0.04)	0.20 (0.04)	0.29 (0.02)	0.45 (0.02)	0.48 (0.03)	0.24 (0.04)	0.37 (0.06)	0.47 (0.05)	0.59 (0.06)
Spotscape (w/o SS)	0.41 (0.01)	0.56 (0.01)	0.69 (0.01)	0.67 (0.02)	0.39 (0.01)	0.53 (0.02)	0.67 (0.01)	0.69 (0.03)	0.39 (0.02)	0.58 (0.06)	0.67 (0.02)	0.75 (0.06)
Spotscape	0.42 (0.01)	0.56 (0.02)	0.69 (0.01)	0.68 (0.02)	0.40 (0.02)	0.53 (0.02)	0.68 (0.01)	0.69 (0.02)	0.40 (0.02)	0.60 (0.04)	0.67 (0.01)	0.76 (0.04)

Table 6: Heterogeneous integration performance on MTG data.

	Clustering Metric				Batch Effect Correction Metric				
	Silhouette	ARI	NMI	CA	Silhouette	Batch	iLISI	kBET	Graph Connectivity
GraphST	0.43 (0.01)	0.23 (0.02)	0.42 (0.00)	0.39 (0.01)	0.56 (0.00)	0.00 (0.00)	0.02 (0.00)	0.65 (0.02)	
STAligner	0.38 (0.03)	0.38 (0.03)	0.54 (0.03)	0.49 (0.02)	0.62 (0.04)	0.16 (0.23)	0.11 (0.08)	0.85 (0.04)	
Spotscape (w/o SS)	0.59 (0.04)	0.40 (0.07)	0.56 (0.03)	0.52 (0.05)	0.25 (0.02)	0.00 (0.00)	0.00 (0.00)	0.64 (0.01)	
Spotscape	0.52 (0.03)	0.68 (0.08)	0.75 (0.02)	0.76 (0.08)	0.69 (0.01)	0.08 (0.04)	0.17 (0.05)	0.88 (0.02)	

Figure 4: UMAP of Raw, GraphST, STAligner, Spotscape (w/o SS), Spotscape by slice, ground truth, and K -means clustering results

To check whether our results yield biologically meaningful results, we investigate differentially expressed genes (DEGs) and their biological functions between the control and Alzheimer’s disease (AD) group through Gene Ontology (GO) enrichment analysis for each cluster, representing a cortical layer in a brain. Since Spotscape provides spatially organized and reliably distributed clusters as actual cortical layers in a brain, all clusters are assigned to the cortical layers. As pathological influence of AD on different cortical layers is diverse, it is highly worthwhile to identify differences between the control and AD in each region (Romito-DiGiacomo et al., 2007). As depicted in Figure 24, in layer 2, which is regarded as a superficial layer, the terms in ‘humoral immune response mediated by circulating immunoglobulin (GO:0002455)’, ‘synapse pruning (GO:0098883)’, and ‘regulation Of histone deacetylase activity (GO:1901725)’ are enriched. On the other hand, layer 5, a deeper layer, enrich terms as ‘synapse pruning (GO:0098883)’, ‘positive regulation of cytokine production (GO:0001819)’, ‘microglial cell activation (GO:0001774)’, and ‘Positive regulation of neuron death (GO:1901216)’, as shown in Figure 25. All of these enriched biological processes are reported to be considerably relevant with AD (Mruthinti et al., 2004; Brucato & Benjamin, 2020; Lu et al., 2015; Wu et al., 2021; Goel et al., 2022). Moreover, the top enriched molecular function in Layer 5 is ‘amyloid-beta binding (GO:0001540)’, supporting reliability of results. Interestingly, synapse pruning and terms related to immune response are remarkably enriched in common, while angiogenesis, known to be associated with amyloid-beta pathway in AD (WA et al., 2013), is only enriched in Layer 2. These observations provide biological insights, namely shared characteristics and difference of AD in distinct cortical layers.

Multi-slice Alignment Results. Finally, we conduct experiments on multi-slice alignments of the Mouse Embryo data, which require alignment results to track the development stages of the embryo. To this end, we match E11.5 and E12.5 and report the Label Transfer ARI (LTARI) in Table 7, which measures the agreement between true labels and the labels assigned through the alignment process, and visualize our results in Figure 5. These results show that Spotscape achieves better alignment than SLAT, which is specifically designed for alignment tasks, demonstrating the general applicability of Spotscape.

Table 7: Alignment performance of Mouse embryo datasets.

	LTARI
STAligner	0.46 (0.02)
scSLAT	0.52 (0.01)
Spotscape	0.56 (0.01)

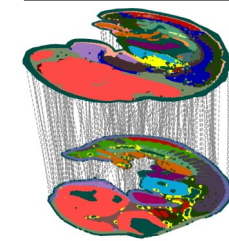
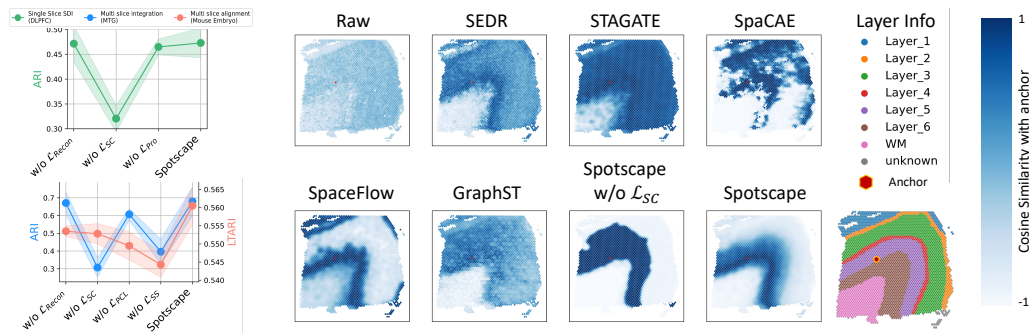


Figure 5: Alignment results of Mouse embryo datasets.

Furthermore, we conduct cross-technology alignment between data obtained from Xenium and Visium. Since Xenium offers higher resolution than Visium, while Visium provides a more comprehensive transcriptome view, aligning Xenium with Visium creates a complementary approach that combines the strengths of both: high resolution and broader coverage. To this end, we align triple-positive cells in Xenium—those positively enriched for the ERBB2, PGR, and ESR1 marker genes associated with breast tumors—with corresponding Visium spots. Figure 6 shows that Spotscape successfully outputs seven aligned points and identifies five triple-positive cells in the Visium data. This demonstrates the superiority of Spotscape, as it can successfully align extremely rare cell types (e.g., cancer cells).

499 5.4 MODEL ANALYSIS

Ablation studies. We also conduct ablation studies on the components of Spotscape to clarify the necessity of each module, as shown in Figure 7. Across all three tasks, our proposed Similarity Telescope (i.e., \mathcal{L}_{SC}) demonstrates its importance by showing a significant performance drop without this module. Additionally, prototypical contrastive learning (i.e., \mathcal{L}_{PCL}) further confirms its role in enhancing representations by consistently showing performance gains. In contrast, the reconstruction loss (i.e., \mathcal{L}_{Recon}) does not demonstrate significant performance gains excluding alignment tasks, since it is only needed for stabilizing the training procedures.



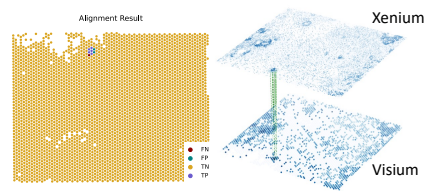
519 Figure 7: Ablation studies.

520 Figure 8: Similarity comparison based on anchor node 489 in Layer 5.

Similarity analysis. As a deeper analysis of Spotscape, we examine whether it successfully learns the relative similarities between spots, which is a key motivation behind our approach. In Figure 8, we randomly select an anchor spot from the DLPFC data and visualize the similarity between the selected anchor and other remaining spots. While other baselines fail to capture appropriate similarities, Spotscape accurately reflects the dynamics of the SRT data with respect to the spatial distance and exhibits varying levels of similarity corresponding to true spatial domain types.

527 6 CONCLUSION

529 In this work, we propose Spotscape, a novel framework for representation learning on the SRT
 530 data that is generally adaptable for both single and multi-slice tasks. The main idea of Spotscape is
 531 that while the spatial locality information is important in the SRT data, it often provides limited
 532 insights due to the continuous nature of this data. Therefore, Spotscape reflects the global similari-
 533 ties between spot representations by preserving a global similarity map invariant to augmentations
 534 during the training process. Moreover, Spotscape enhances spot representations by introducing the
 535 prototypical contrastive learning scheme into the SRT data to learn more fine-grained spot represen-
 536 tations. Furthermore, we introduce a simple batch effect reduction strategy called similarity scaling,
 537 which explicitly regulates the scale of similarities to maintain consistency across spots located in
 538 different samples for extending applications of Spotscape to multi-slice tasks. Extensive exper-
 539 iments demonstrate that Spotscape outperforms existing baselines across SRT data from various
 platforms and diverse downstream tasks. Furthermore, we show that results from Spotscape can
 assist biologically meaningful findings, highlighting its future potential for practical SRT analysis.

550 Figure 6: Alignment results of triple
 551 positive cells.

540 REFERENCES
541

- 542 Miri Adler, Yael Korem Kohanim, Avichai Tendler, Avi Mayo, and Uri Alon. Continuum of gene-
543 expression profiles provides spatial division of labor within a differentiated cell type. *Cell systems*,
544 8(1):43–52, 2019.
- 545 Rohit Arora, Christian Cao, Mehul Kumar, Sarthak Sinha, Ayan Chanda, Reid McNeil, Divya
546 Samuel, Rahul K Arora, T Wayne Matthews, Shamir Chandarana, et al. Spatial transcriptomics
547 reveals distinct and conserved tumor core and edge architectures that predict survival and targeted
548 therapy response. *Nature Communications*, 14(1):5029, 2023.
- 549 Dharmesh D Bhuva, Chin Wee Tan, Agus Salim, Claire Marceaux, Marie A Pickering, Jinjin Chen,
550 Malvika Kharbanda, Xinyi Jin, Ning Liu, Kristen Feher, et al. Library size confounds biology in
551 spatial transcriptomics data. *Genome Biology*, 25(1):99, 2024.
- 552 Vincent D Blondel, Jean-Loup Guillaume, Renaud Lambiotte, and Etienne Lefebvre. Fast unfolding
553 of communities in large networks. *Journal of statistical mechanics: theory and experiment*, 2008
554 (10):P10008, 2008.
- 555 Dr. Rick Brucato and Daniel E. Benjamin. Synaptic pruning in alzheimer’s disease: Role of the com-
556 plement system. *Global Journal of Medical Research*, 20(F6):1–20, May 2020. URL <https://medicalresearchjournal.org/index.php/GJMR/article/view/2113>.
- 557 Mathilde Caron, Ishan Misra, Julien Mairal, Priya Goyal, Piotr Bojanowski, and Armand Joulin.
558 Unsupervised learning of visual features by contrasting cluster assignments. *Advances in neural
559 information processing systems*, 33:9912–9924, 2020a.
- 560 Mathilde Caron, Ishan Misra, Julien Mairal, Priya Goyal, Piotr Bojanowski, and Armand Joulin.
561 Unsupervised learning of visual features by contrasting cluster assignments. *Advances in neural
562 information processing systems*, 33:9912–9924, 2020b.
- 563 Mark S Cembrowski and Vilas Menon. Continuous variation within cell types of the nervous system.
564 *Trends in Neurosciences*, 41(6):337–348, 2018.
- 565 Ao Chen, Sha Liao, Mengnan Cheng, Kailong Ma, Liang Wu, Yiwei Lai, Xiaojie Qiu, Jin Yang,
566 Jiangshan Xu, Shijie Hao, et al. Spatiotemporal transcriptomic atlas of mouse organogenesis
567 using dna nanoball-patterned arrays. *Cell*, 185(10):1777–1792, 2022a.
- 568 Shuo Chen, Yuzhou Chang, Liangping Li, Diana Acosta, Yang Li, Qi Guo, Cankun Wang, Emir
569 Turkes, Cody Morrison, Dominic Julian, et al. Spatially resolved transcriptomics reveals genes
570 associated with the vulnerability of middle temporal gyrus in alzheimer’s disease. *Acta Neu-
571 ropathologica Communications*, 10(1):188, 2022b.
- 572 Ting Chen, Simon Kornblith, Mohammad Norouzi, and Geoffrey Hinton. A simple framework for
573 contrastive learning of visual representations. In *International conference on machine learning*,
574 pp. 1597–1607. PMLR, 2020.
- 575 Erin A Clark, Michael Rutlin, Lucia S Capano, Samuel Aviles, Jordan R Saadon, Praveen Taneja,
576 Qiyu Zhang, James B Bullis, Timothy Lauer, Emma Myers, et al. Cortical ror β is required for
577 layer 4 transcriptional identity and barrel integrity. *Elife*, 9:e52370, 2020.
- 578 Siavash Fazel Darbandi, Sarah E Robinson Schwartz, Qihao Qi, Rinaldo Catta-Preta, Emily Ling-
579 Lin Pai, Jeffrey D Mandell, Amanda Everitt, Anna Rubin, Rebecca A Krasnoff, Sol Katzman,
580 et al. Neonatal tbr1 dosage controls cortical layer 6 connectivity. *Neuron*, 100(4):831–845, 2018.
- 581 Carlo De Donno, Soroor Hediyyeh-Zadeh, Amir Ali Moinfar, Marco Wagenstetter, Luke Zappia,
582 Mohammad Lotfollahi, and Fabian J Theis. Population-level integration of single-cell datasets
583 enables multi-scale analysis across samples. *Nature Methods*, 20(11):1683–1692, 2023.
- 584 Kangning Dong and Shihua Zhang. Deciphering spatial domains from spatially resolved transcrip-
585 toomics with an adaptive graph attention auto-encoder. *Nature communications*, 13(1):1739, 2022.
- 586 Ruben Dries, Qian Zhu, Rui Dong, Chee-Huat Linus Eng, Huipeng Li, Kan Liu, Yuntian Fu, Tianx-
587 iao Zhao, Arpan Sarkar, Feng Bao, et al. Giotto: a toolbox for integrative analysis and visualiza-
588 tion of spatial expression data. *Genome biology*, 22:1–31, 2021.

- 594 Parul Goel, Sasanka Chakrabarti, Kapil Goel, Karanpreet Bhutani, Tanya Chopra, and Sha-
 595 radendu Bali. Neuronal cell death mechanisms in alzheimer's disease: An insight. *Frontiers*
 596 in *Molecular Neuroscience*, 15, 2022. ISSN 1662-5099. doi: 10.3389/fnmol.2022.937133.
 597 URL <https://www.frontiersin.org/journals/molecular-neuroscience/articles/10.3389/fnmol.2022.937133>.
- 598
 599 Thomas M Goralski, Lindsay Meyerdirk, Libby Breton, Laura Brasseur, Kevin Kurgat, Daniella
 600 DeWeerd, Lisa Turner, Katelyn Becker, Marie Adams, Daniel J Newhouse, et al. Spatial tran-
 601 scriptomics reveals molecular dysfunction associated with cortical lewy pathology. *Nature Com-*
 602 *munications*, 15(1):2642, 2024.
- 603
 604 Jean-Bastien Grill, Florian Strub, Florent Altché, Corentin Tallec, Pierre Richemond, Elena
 605 Buchatskaya, Carl Doersch, Bernardo Avila Pires, Zhaohan Guo, Mohammad Gheshlaghi Azar,
 606 et al. Bootstrap your own latent-a new approach to self-supervised learning. *Advances in neural*
 607 *information processing systems*, 33:21271–21284, 2020.
- 608
 609 Yuhao Hao, Stephanie Hao, Erica Andersen-Nissen, William M Mauck, Shiwei Zheng, Andrew
 610 Butler, Maddie J Lee, Aaron J Wilk, Charlotte Darby, Michael Zager, et al. Integrated analysis of
 611 multimodal single-cell data. *Cell*, 184(13):3573–3587, 2021.
- 612
 613 Yuhao Hao, Tim Stuart, Madeline H Kowalski, Saket Choudhary, Paul Hoffman, Austin Hartman,
 614 Avi Srivastava, Gesmira Molla, Shaista Madad, Carlos Fernandez-Granda, and Rahul Satija. Dic-
 615 tionary learning for integrative, multimodal and scalable single-cell analysis. *Nature Biotech-*
 616 *nology*, 2023. doi: 10.1038/s41587-023-01767-y. URL <https://doi.org/10.1038/s41587-023-01767-y>.
- 617
 618 Benjamin D Harris, Megan Crow, Stephan Fischer, and Jesse Gillis. Single-cell co-expression anal-
 619 ysis reveals that transcriptional modules are shared across cell types in the brain. *Cell systems*, 12
 620 (7):748–756, 2021.
- 621
 622 Jian Hu, Xiangjie Li, Kyle Coleman, Amelia Schroeder, Nan Ma, David J Irwin, Edward B Lee,
 623 Russell T Shinohara, and Mingyao Li. Spagn: Integrating gene expression, spatial location and
 624 histology to identify spatial domains and spatially variable genes by graph convolutional network.
Nature methods, 18(11):1342–1351, 2021.
- 625
 626 Yaofeng Hu, Kai Xiao, Hengyu Yang, Xiaoping Liu, Chuanchao Zhang, and Qianqian Shi. Spatially
 627 contrastive variational autoencoder for deciphering tissue heterogeneity from spatially resolved
 628 transcriptomics. *Briefings in Bioinformatics*, 25(2):bbae016, 2024.
- 629
 630 Amanda Janesick, Robert Shelansky, Andrew D Gottscho, Florian Wagner, Stephen R Williams,
 631 Morgane Rouault, Ghezal Beliakoff, Carolyn A Morrison, Michelli F Oliveira, Jordan T Sicher-
 632 man, et al. High resolution mapping of the tumor microenvironment using integrated single-cell,
 633 spatial and in situ analysis. *Nature Communications*, 14(1):8353, 2023.
- 634
 635 Thomas N Kipf and Max Welling. Semi-supervised classification with graph convolutional net-
 636 works. *arXiv preprint arXiv:1609.02907*, 2016.
- 637
 638 Junseok Lee, Sungwon Kim, Dongmin Hyun, Namkyeong Lee, Yejin Kim, and Chanyoung Park.
 Deep single-cell rna-seq data clustering with graph prototypical contrastive learning. *Bioinfor-*
 639 *matics*, 39(6):btad342, 2023.
- 640
 641 Junseok Lee, Sukwon Yun, Yeongmin Kim, Tianlong Chen, Manolis Kellis, and Chanyoung Park.
 Single-cell rna sequencing data imputation using bi-level feature propagation. *Briefings in Bioin-*
 642 *formatics*, 25(3):bbae209, 2024.
- 643
 644 Junnan Li, Pan Zhou, Caiming Xiong, and Steven CH Hoi. Prototypical contrastive learning of
 645 unsupervised representations. *arXiv preprint arXiv:2005.04966*, 2020a.
- 646
 647 Xiangjie Li, Kui Wang, Yafei Lyu, Huize Pan, Jingxiao Zhang, Dwight Stambolian, Katalin Susztak,
 Muredach P Reilly, Gang Hu, and Mingyao Li. Deep learning enables accurate clustering with
 batch effect removal in single-cell rna-seq analysis. *Nature communications*, 11(1):2338, 2020b.

- 648 Yahui Long, Kok Siong Ang, Mengwei Li, Kian Long Kelvin Chong, Raman Sethi, Chengwei
 649 Zhong, Hang Xu, Zhiwei Ong, Karishma Sachaphibulkij, Ao Chen, et al. Spatially informed
 650 clustering, integration, and deconvolution of spatial transcriptomics with graphst. *Nature Com-*
 651 *munications*, 14(1):1155, 2023.
- 652 Xi Lu, Li Wang, Caijia Yu, Daohai Yu, and Gang Yu. Histone acetylation modifiers in the patho-
 653 genesis of alzheimer’s disease. *Frontiers in Cellular Neuroscience*, 9, 2015. ISSN 1662-5102.
 654 doi: 10.3389/fncel.2015.00226. URL <https://www.frontiersin.org/journals/cellular-neuroscience/articles/10.3389/fncel.2015.00226>.
- 655
- 656 Eric Lubeck, Ahmet F Coskun, Timur Zhiyentayev, Mubhij Ahmad, and Long Cai. Single-cell in
 657 situ rna profiling by sequential hybridization. *Nature methods*, 11(4):360–361, 2014.
- 658
- 659 Kristen R Maynard, Leonardo Collado-Torres, Lukas M Weber, Cedric Uytingco, Brianna K Barry,
 660 Stephen R Williams, Joseph L Catallini, Matthew N Tran, Zachary Besich, Madhavi Tippani,
 661 et al. Transcriptome-scale spatial gene expression in the human dorsolateral prefrontal cortex.
 662 *Nature neuroscience*, 24(3):425–436, 2021.
- 663 Shyamala Mruthinti, Jerry J Buccafusco, William D Hill, Jennifer L Waller, Thomas W Jack-
 664 son, Edward Y Zamrini, and Rosann F Schade. Autoimmunity in alzheimer’s disease: in-
 665 creased levels of circulating iggs binding amyloid beta and rage peptides. *Neurobiology of Ag-*
 666 *ing*, 25(8):1023–1032, 2004. ISSN 0197-4580. doi: <https://doi.org/10.1016/j.neurobiolaging.2003.11.001>. URL <https://www.sciencedirect.com/science/article/pii/S0197458003002215>.
- 667
- 668 James W Phillips, Anton Schulmann, Erina Hara, Johan Winnubst, Chenghao Liu, Vera Valakh,
 669 Lihua Wang, Brenda C Shields, Wyatt Korff, Jayaram Chandrashekhar, et al. A repeated molecular
 670 architecture across thalamic pathways. *Nature neuroscience*, 22(11):1925–1935, 2019.
- 671
- 672 Honglei Ren, Benjamin L Walker, Zixuan Cang, and Qing Nie. Identifying multicellular spatiotem-
 673 poral organization of cells with spaceflow. *Nature communications*, 13(1):4076, 2022.
- 674
- 675 Rita R. Romito-DiGiacomo, Harry Menegay, Samantha A. Cicero, and Karl Herrup. Effects of
 676 alzheimer’s disease on different cortical layers: The role of intrinsic differences in amyloid beta
 677 susceptibility. *Journal of Neuroscience*, 27(32):8496–8504, 2007. ISSN 0270-6474. doi: 10.
 678 1523/JNEUROSCI.1008-07.2007. URL <https://www.jneurosci.org/content/27/32/8496>.
- 679
- 680 Tim Stuart, Andrew Butler, Paul Hoffman, Christoph Hafemeister, Efthymia Papalexi, William M
 681 Mauck, Yuhan Hao, Marlon Stoeckius, Peter Smibert, and Rahul Satija. Comprehensive integra-
 682 tion of single-cell data. *cell*, 177(7):1888–1902, 2019.
- 683
- 684 Shantanu Thakoor, Corentin Tallec, Mohammad Gheshlaghi Azar, Mehdi Azabou, Eva L Dyer,
 685 Remi Munos, Petar Veličković, and Michal Valko. Large-scale representation learning on graphs
 686 via bootstrapping. *arXiv preprint arXiv:2102.06514*, 2021.
- 687
- 688 Petar Veličković, Guillem Cucurull, Arantxa Casanova, Adriana Romero, Pietro Liò, and Yoshua
 689 Bengio. Graph attention networks. *arXiv preprint arXiv:1710.10903*, 2017.
- 690
- 691 Petar Veličković, William Fedus, William L Hamilton, Pietro Liò, Yoshua Bengio, and R Devon
 692 Hjelm. Deep graph infomax. *arXiv preprint arXiv:1809.10341*, 2018.
- 693
- 694 Jefferies WA, Price KA, Biron KE, Fenninger F, Pfeifer CG, and Dickstein DL. Adjusting the
 695 compass: new insights into the role of angiogenesis in alzheimer’s disease. *Alzheimer’s Research
 696 and Therapy*, 2013.
- 697
- 698 Amélie Wegener, Cyrille Deboux, Corinne Bachelin, Magali Frah, Christophe Kerninon, Danielle
 699 Seilhean, Matthias Weider, Michael Wegner, and Brahim Nait-Oumesmar. Gain of olig2 function
 700 in oligodendrocyte progenitors promotes remyelination. *Brain*, 138(1):120–135, 2015.
- 701
- F Alexander Wolf, Philipp Angerer, and Fabian J Theis. Scanpy: large-scale single-cell gene ex-
 702 pression data analysis. *Genome biology*, 19:1–5, 2018a.
- F Alexander Wolf, Philipp Angerer, and Fabian J Theis. Scanpy: large-scale single-cell gene ex-
 703 pression data analysis. *Genome biology*, 19:1–5, 2018b.

- 702 Kai-Min Wu, Ya-Ru Zhang, Yu-Yuan Huang, Qiang Dong, Lan Tan, and Jin-Tai Yu. The
 703 role of the immune system in alzheimer’s disease. *Ageing Research Reviews*, 70:101409,
 704 2021. ISSN 1568-1637. doi: <https://doi.org/10.1016/j.arr.2021.101409>. URL <https://www.sciencedirect.com/science/article/pii/S1568163721001562>.
- 705
- 706 Chen-Rui Xia, Zhi-Jie Cao, Xin-Ming Tu, and Ge Gao. Spatial-linked alignment tool (slat) for
 707 aligning heterogenous slices. *Nature Communications*, 14(1):7236, 2023.
- 708
- 709 Junyuan Xie, Ross Girshick, and Ali Farhadi. Unsupervised deep embedding for clustering analysis.
 710 In *International conference on machine learning*, pp. 478–487. PMLR, 2016.
- 711
- 712 Hang Xu, Huazhu Fu, Yahui Long, Kok Siong Ang, Raman Sethi, Kelvin Chong, Mengwei Li, Rom
 713 Uddamvathanak, Hong Kai Lee, Jingjing Ling, et al. Unsupervised spatially embedded deep
 714 representation of spatial transcriptomics. *Genome Medicine*, 16(1):12, 2024.
- 715
- 716 Ron Zeira, Max Land, Alexander Strzalkowski, and Benjamin J Raphael. Alignment and integration
 717 of spatial transcriptomics data. *Nature Methods*, 19(5):567–575, 2022.
- 718
- 719 Edward Zhao, Matthew R Stone, Xing Ren, Jamie Guenthoer, Kimberly S Smythe, Thomas Pul-
 720 liam, Stephen R Williams, Cedric R Uytingco, Sarah EB Taylor, Paul Nghiem, et al. Spatial
 721 transcriptomics at subspot resolution with bayesspace. *Nature biotechnology*, 39(11):1375–1384,
 722 2021.
- 723
- 724 Xiang Zhou, Kangning Dong, and Shihua Zhang. Integrating spatial transcriptomics data across
 725 different conditions, technologies and developmental stages. *Nature Computational Science*, 3
 726 (10):894–906, 2023.
- 727
- 728
- 729
- 730
- 731
- 732
- 733
- 734
- 735
- 736
- 737
- 738
- 739
- 740
- 741
- 742
- 743
- 744
- 745
- 746
- 747
- 748
- 749
- 750
- 751
- 752
- 753
- 754
- 755

Supplementary Material

- *Global Context-aware Representation Learning for Spatially Resolved Transcriptomics* -

A Datasets	16
B Baseline Methods	17
C Pseudo Code	18
D Sensitivity Analysis	19
E Hyperparameter Selection and Implementation Details	22
E.1 Hyperparamter search for model performance comparison	22
E.2 Unsupervised Hyperparameter Search Strategy	22
E.3 Implementation Details	23
F Scalability of Spotscape	24
G Differentially expressed gene analysis	25
H Trajectory analysis	26
I Imputation	27
J Future works	28

756
757
758
759
760
761
762
763
764
765
766
767
768
769
770
771
772
773
774
775
776
777
778
779
780
781
782
783
784
785
786
787
788
789
790
791
792
793
794
795
796
797
798
799
800
801
802
803
804
805
806
807
808
809

810 **A DATASETS**
 811
 812

813 **Table 8: Statistics for datasets used for experiments.**

Data	Species	Tissue	Technology	Resolution	Cells/Spots	Genes	# of Spatial Domains	Reference
DLPFC	Human	Brain (dorsolateral prefrontal cortex; DLPFC)	10x Visium	50 μ m	3460 ~ 4789	33538	5 ~ 7	(Maynard et al., 2021)
MTG	Human	Brain (middle temporal gyrus; MTG)	10x Visium	50 μ m	3445 ~ 4832	36601	6 ~ 7	(Chen et al., 2022b)
Mouse Embryo	Mouse	Whole embryo	Stereo-seq	0.2 μ m	30756 ~ 55295	25485 ~ 27330	18~19	(Chen et al., 2022a)
NSCLC	Human	Non-small cell lung cancer (NSCLC)	CosMX	Subcellular	960	11756	4	(Bhuvva et al., 2024)
Breast Cancer	Human	Breast Cancer	10x Visium	50 μ m	4992	18085	11	(Janesick et al., 2023)
Breast Cancer	Human	Breast Cancer	10x Xenium	Subcellular	167780	313	20	(Janesick et al., 2023)

814
 815
 816
 817
 818
 819
 820 In this section, we compare Spotscape with baseline methods on various datasets. The data statistics are in Table 8.
 821

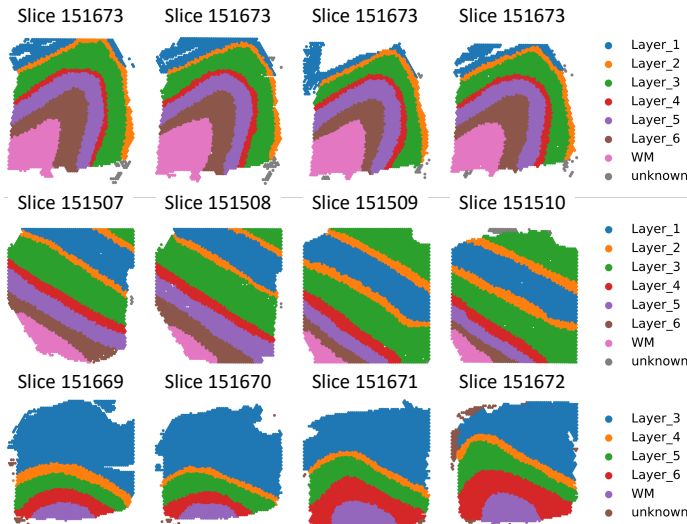
822 **Human Dorsolateral Prefrontal Cortex (DLPFC).** It comprises 12 tissue slices from 3 adult samples, with 4 consecutive slices per sample, derived from the dorsolateral prefrontal cortex. These slices were profiled using the 10x Visium platform. The original study manually annotated 6 neocortical layers (layers 1 to 6) as well as the white matter (see Figure 9).

823
 824
 825
 826 **Middle Temporal Gyrus (MTG).** The MTG (middle temporal gyrus) dataset includes samples from both control and Alzheimer’s disease (AD) groups. The MTG is a brain region particularly vulnerable to early AD pathology. In the original study, spatial transcriptomics profiles were characterized for both AD and control MTG samples by the 6 neocortical layers (layer 1 to 6) and white matter, utilizing the 10x Visium platform for detailed tissue profiling. The spot distribution is denoted in Figure 10.

827
 828
 829
 830
 831 **Mouse Embryo.** It is mouse whole embryo datasets by development stages. It was profiled by Stereo-seq technology, which allows spatial transcriptomics at the cellular level by integrating DNA nanoball-patterned arrays with in situ RNA capture. It offers a detailed spatiotemporal transcriptomic atlas (MOSTA) of mouse embryonic development (see Figure 12).

832
 833
 834
 835 **Non-small cell lung cancer (NSCLC).** The dataset comprises high-resolution, subcellular-level spatial transcriptomics data from human lung tissue, encompassing four distinct spatial domains (see Figure 11), including a tumor region. This data was generated using the NanoString CosMX platform.

836
 837
 838
 839 **Human Breast Cancer.** It comprises spatial transcriptomics of human breast cancer tissues using 10x Visium for whole-transcriptome spatial data and 10x Xenium for high-resolution gene expression at the subcellular level. This combined approach offers detailed mapping of tumor microenvironments (see Figure 6), highlighting molecular differences and cell-type composition to better understand cancer heterogeneity and invasion.



840
 841
 842
 843
 844
 845
 846 **Figure 9: Spatial coordinates of DLPFC dataset.**

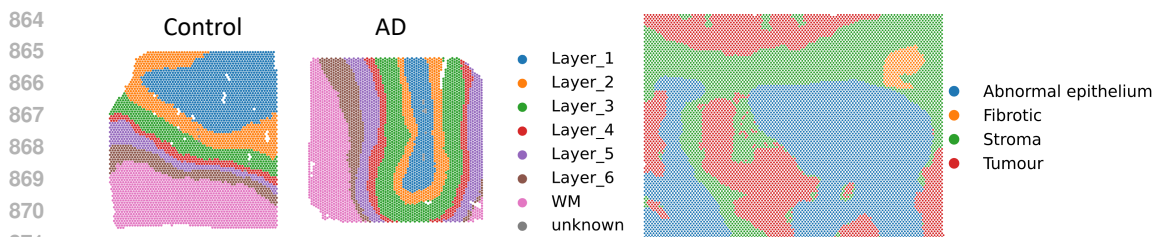


Figure 10: Spatial coordinates of MTG dataset. Figure 11: Spatial coordinates of NSCLC dataset.

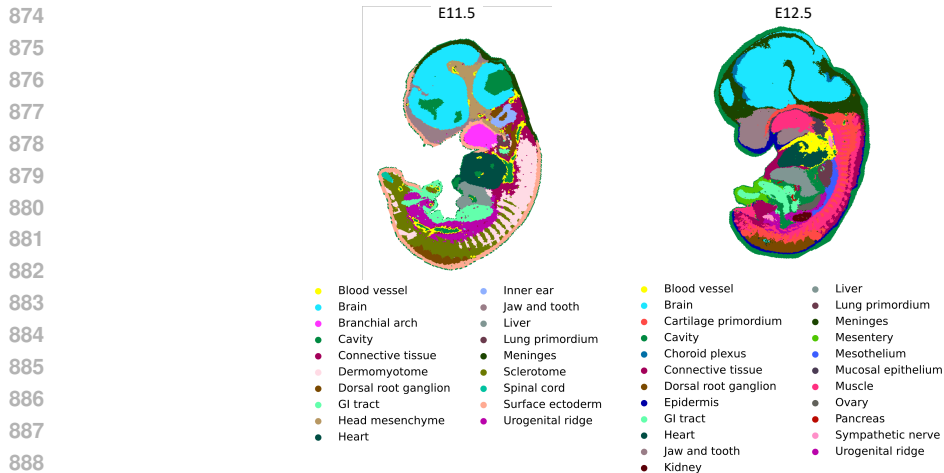


Figure 12: Spatial coordinates of Mouse Development dataset.

B BASELINE METHODS

In Table 9, we indicate which baseline methods are applicable to specific tasks, categorizing them based on whether their respective papers address those problems. Furthermore, we compare the performance of Spotscape with general self-supervised representation learning schemes. Graph Contrastive Learning (Chen et al., 2020; Zhu et al., 2020) is a instance-wise contrastive learning method that learns representations by pushing negative pairs apart and pulling positive pairs together. BGRL (Thakoor et al., 2021; Grill et al., 2020) is a consistency regularization method that learns representations by enforcing consistency between two differently augmented views. SwAV (Caron et al., 2020b) learns representations by minimizing the difference between two cluster assignments that are obtained through optimal transport. Barlow twins (Caron et al., 2020a) learns representations by minimizing redundancy between two augmented view. Although these methods demonstrate strong performance across various domains, our results in Figure 13 indicate that Spotscape is the most suitable model for SRT data, emphasizing its effectiveness in this context.

Table 9: Baseline methods and their application across various tasks

Method	Single-slice SDI	Homogeneous integration	Homogeneous alignment	Heterogeneous integration	Heterogeneous alignment
SEDR	✓				
STAGATE	✓				
Spotscape	✓				
SpaceFlow	✓				
GraphST	✓				
PASTIE		✓	✓		
STAigner		✓	✓		
SLAT		✓	✓	✓	✓
Spotscape	✓	✓	✓	✓	✓

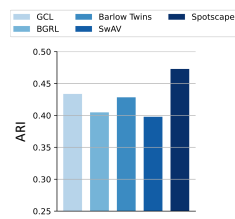


Figure 13: Comparison with self-supervised learning

918 C PSEUDO CODE

In this section, we provide pseudocode of Spotscape in Algorithm 1.

Algorithm 1 Overall framework of Spotscape

Require: Spatial nearest neighbor graph $\mathcal{G} = (X, A)$, feature matrix X , adjacency matrix A , graph augmentation \mathcal{T} , GCN encoder f_θ , decoder g_θ , number of slices N_d , number of spots N_s , number of latent dimensions D , loss balancing parameters $(\lambda_{Recon}, \lambda_{SC}, \lambda_{PCL}, \lambda_{SS})$, temperature τ , learning rate η
Ensure: Node embeddings Z , reconstructed feature matrix \hat{X}

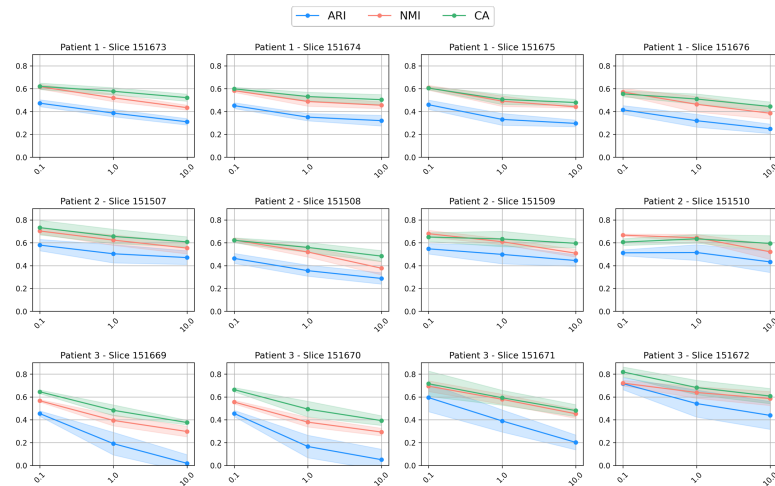
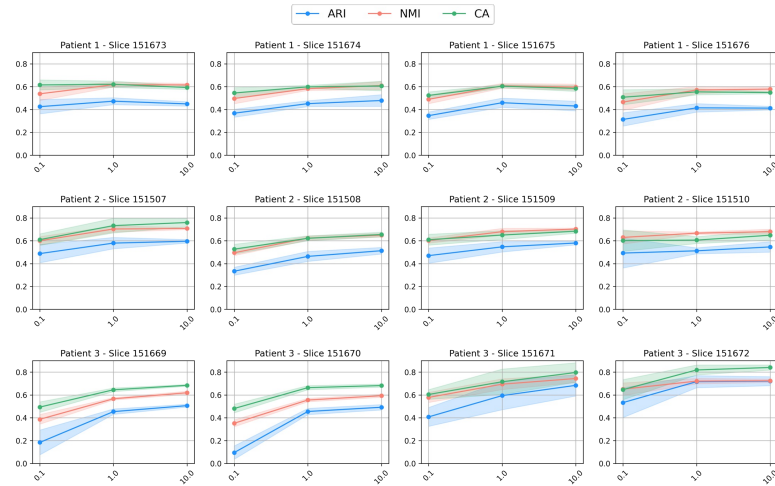
Ensure: Node embeddings Z , reconstructed feature matrix X

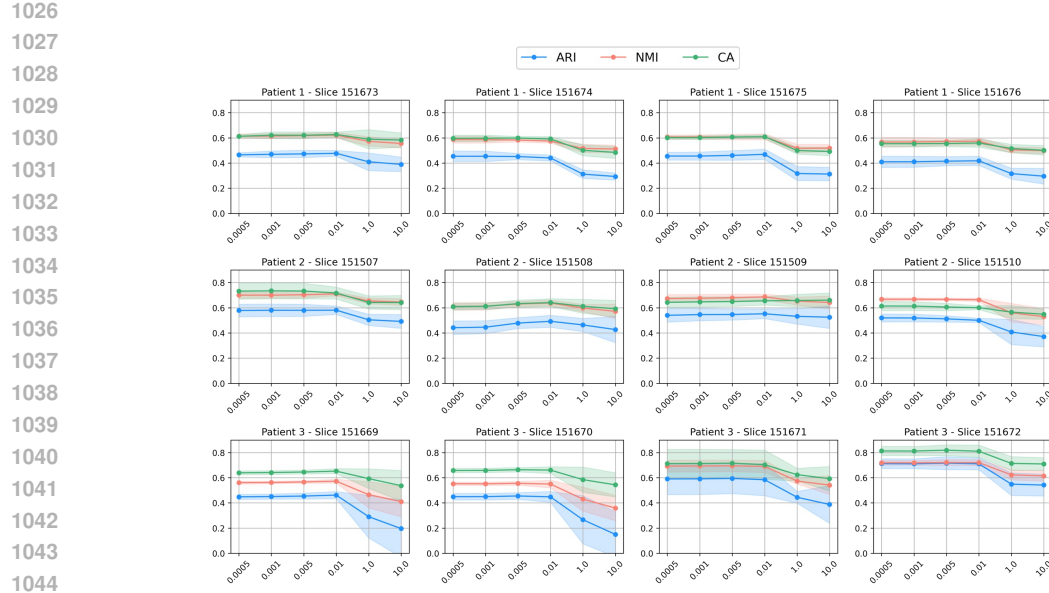
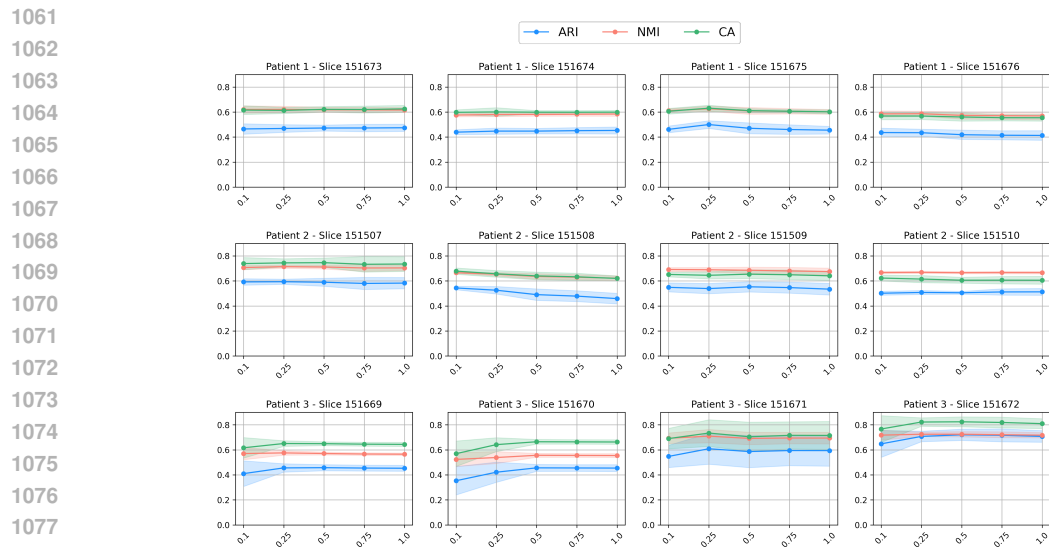
```

928 1: for epoch in epochs:
929 2:    $\tilde{\mathcal{G}}, \tilde{\mathcal{G}}' = \mathcal{T}(\mathcal{G})$                                      /* two randomly augmented version of G */
930 3:   Step 1: Graph Autoencoder
931 4:    $\tilde{Z} = f_{\theta}(\mathcal{G}), \tilde{Z}' = f_{\theta}(\tilde{\mathcal{G}})$            /* compute spot embedding using GNN encoder */
932 5:    $\hat{X} = g_{\theta}(\tilde{Z}), \hat{X}' = g_{\theta}(\tilde{Z}')$           /* reconstruct the feature matrix using decoder */
933 6:   Step 2: Similarity Telescope with Relation Consistency (Section 4.2)
934 7:    $\mathcal{L}_{Recon} = \text{Reconstruction Loss}(X, \hat{X}, \hat{X}')$           (Eqn. 2)
935 8:    $\mathcal{L}_{SC}, H = \text{Similarity Telescope with Relation Consistency Loss}(\tilde{Z}, \tilde{Z}')$ 
936
937 9:   Step 3: Prototypical Contrastive Learning (Section 4.3)
938 10:  if epoch  $\geq$  warm-up epoch then
939 11:     $\mathcal{L}_{PCL} = \text{PCL Loss}(\tilde{Z}, \tilde{Z}')$ 
940 12:  else
941 13:     $\mathcal{L}_{PCL} = 0$ 
942 14:  end if
943 15:  Step 4: Similarity Scaling Strategy (Section 4.4)
944 16:  if  $N_d \geq 2$  then
945 17:     $\mathcal{L}_{SS} = \text{Similarity Scaling Loss}(H, \mathcal{G})$           (Eqn. 7)
946 18:  else
947 19:     $\mathcal{L}_{SS} = 0$ 
948 20:  end if
949 21:  Step 5: Compute Loss
950 22:   $\mathcal{L} = \lambda_{Recon}\mathcal{L}_{Recon} + \lambda_{SC}\mathcal{L}_{SC} + \lambda_{PCL}\mathcal{L}_{PCL} + \lambda_{SS}\mathcal{L}_{SS}$ 
951 23:  Step 6: Backpropagation and Parameter Update
952 24:  Update parameters  $\theta$  using Adam optimizer:  $\theta_{epoch} \leftarrow \text{Adam}(\theta_{epoch-1}, \eta)$ 
953 25: Return: Node embeddings  $Z$ , reconstructed feature matrix  $\hat{X}$ 
954 26: /* Utility Functions */
955 27: Function Similarity Telescope with Relation Consistency Loss( $\tilde{Z}, \tilde{Z}'$ ):          /* L2-normalization */
956 28:    $\tilde{Z}_{norm} = \text{L2-norm}(\tilde{Z}), \tilde{Z}'_{norm} = \text{L2-norm}(\tilde{Z}')$ 
957 29:    $H = \tilde{Z}_{norm} \cdot (\tilde{Z}'_{norm})^T, H' = \tilde{Z}'_{norm} \cdot (\tilde{Z}_{norm})^T$           /* compute cosine similarity */
958 30:    $\mathcal{L}_{SC} = \text{MSE}(H, H')$                                               (Eqn. 1)
959 31: Function PCL Loss( $\tilde{Z}, \tilde{Z}'$ ):
960 32:   #  $P_{set}$ : the collection of prototype sets from K-means clustering
961 33:    $P_{set} \leftarrow \text{Assign Prototype}(\tilde{Z}')$ 
962 34:   Calculate the prototypical contrastive loss  $\mathcal{L}_{PCL}$  using  $\tilde{Z}$  and  $P_{set}$           (Eqn. 4)
963 35:   Return:  $\mathcal{L}_{PCL}$ 
964 36: Function Assign Prototype( $Z$ ):
965 37:    $P_{set} \leftarrow []$ 
966 38:   for  $K$  in  $[K^1, K^2, \dots, K^T]$ :
967 39:     Cluster each cell into  $K$  clusters based on  $Z$ 
968 40:     Compute a prototype matrix  $P \in \mathbb{R}^{K \times D}$  by averaging of the spot embeddings per cluster
969 41:     Append  $P$  to  $P_{set}$ 
970 42:   Return:  $P_{set}$ 

```

972 D SENSITIVITY ANALYSIS
973

974 We conduct a sensitivity analysis on all four balancing parameters λ_{Recon} , λ_{SC} , λ_{PCL} , and λ_{SS}
975 in Figure 14, 15, 16, and 17, respectively. In the case of the reconstruction loss (λ_{Recon}), when its
976 weight is too high, performance tends to degrade, indicating that it serves primarily as an auxiliary
977 loss to prevent degenerate solutions. On the other hand, the relation consistency loss (λ_{SC}) shows a
978 degradation in performance when its weight is too small, emphasizing the importance of reflecting
979 global similarities through this loss in **Spotscape**. Prototypical contrastive learning (λ_{PCL}) is
980 robust within a reasonable search space and does not dominate the overall training process. However,
981 it leads to significant performance drops when its weight is too high. Finally, similarity scaling
982 (λ_{SS}) shows robust performance across a wide range of values, with slightly improved performance
983 at higher weights. Furthermore, we conduct a sensitivity analysis for the manually tuned parameters,
984 namely τ and the learning rate, as shown in Figures 18, and 19. We observe that τ shows generally
985 robust performance, while the learning rate fluctuates significantly without a clear trend. These
986 results provide insight that, except for the learning rate, other hyperparameters exhibit robustness
987 within a reasonable search space, suggesting that **Spotscape** requires some learning rate search
988 strategies.
989

1005 Figure 14: Sensitivity analysis for reconstruction loss balancing parameter (λ_{Recon}) of single
1006 DLPFC.
1007

1024 Figure 15: Sensitivity analysis for similarity telescope loss balancing parameter (λ_{SC}) of single
1025 DLPFC.
1026

Figure 16: Sensitivity analysis for balancing parameter of PCL (λ_{PCL}) of single DLPFC.Figure 17: Sensitivity analysis for balancing parameter of similarity scaling (λ_{SS}) of MTG.

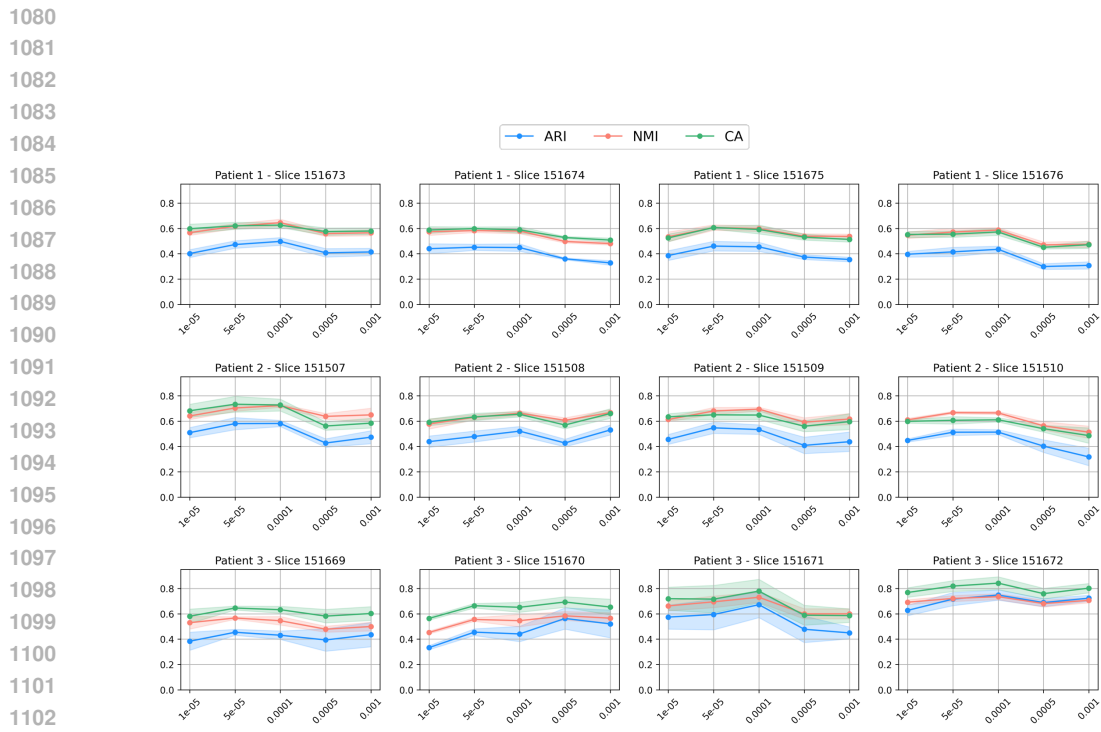


Figure 19: Sensitivity analysis for learning rate of single DLPFC.

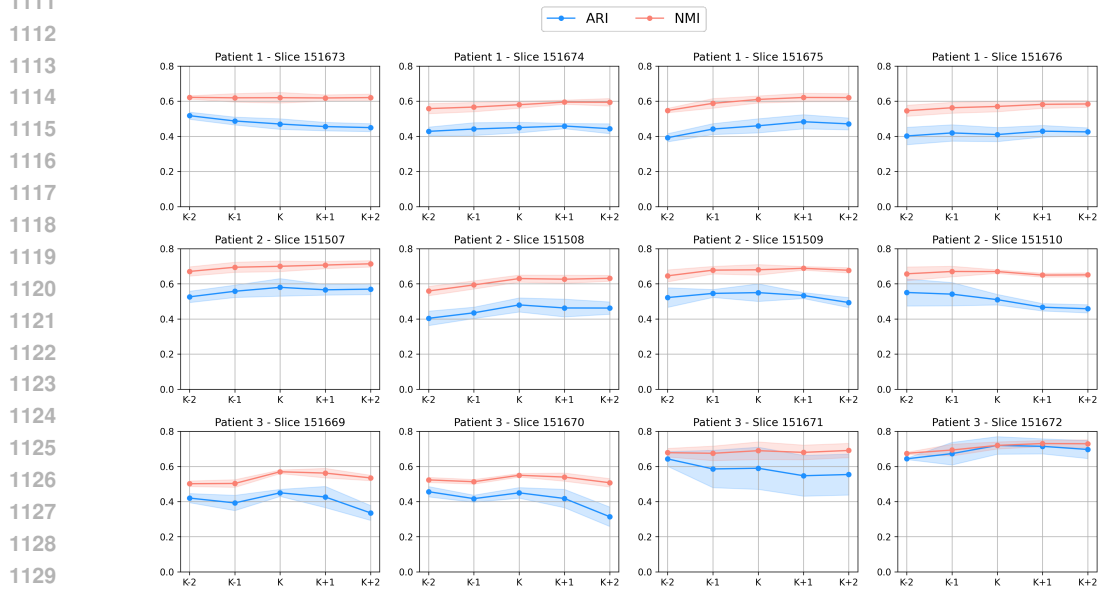


Figure 20: Sensitivity analysis for number of cluster (K) of single DLPFC.

1134 E HYPERPARAMETER SELECTION AND IMPLEMENTATION DETAILS

1135 E.1 HYPERPARAMTER SEARCH FOR MODEL PERFORMANCE COMPARISON

1136 To ensure a fair comparison, we conducted a hyperparameter search for both Spotscape and the
 1137 baseline methods. The best-performing hyperparameters were selected by evaluating the NMI with
 1138 the first seed. Specifically, for Spotscape, the hyperparameter search spaces were defined as fol-
 1139 lows: for λ_{PCL} , the values considered were $\{0.0005, 0.001, 0.005, 0.01\}$; for λ_{SS} , the range in-
 1140 cluded $\{0.1, 1.0, 10.0\}$. The temperature (τ) in PCL was explored over $\{0.1, 0.25, 0.5, 0.75, 1.0\}$,
 1141 and the learning rate search space consisted of $\{0.00001, 0.00005, 0.0001, 0.0005, 0.001\}$. The re-
 1142 maining hyperparameters were fixed, and the ones used to report the experimental results are listed
 1143 in Table 10.

1144 **Table 10: Hyperparameter settings of Spotscape**

	Fixed	DLPFC Single	MTG Single	Mouse Embryo	DLPFC Multi Integration	MTG Multi Integration	Mouse Embryo Alignment	Visium - Xenium Alignment
λ_{Recon}	✓	0.1	0.1	0.1	0.1	0.1	0.1	0.1
λ_{SC}		1.0	1.0	1.0	1.0	1.0	1.0	1.0
λ_{PCL}	0.005	0.0005	0.0005	0.0005	0.005	0.01	0.01	0.01
λ_{SS}	N/A	N/A	N/A	N/A	0.1	10.0	1.0	1.0
GCN encoder dimensions	✓	[256, 64]	[256, 64]	[256, 64]	[256, 64]	[256, 64]	[256, 64]	[256, 64]
τ	0.75	1.0	0.1	0.5	0.5	0.5	0.5	0.5
Top-k	✓	5	5	5	5	3	5	5
Training epochs	✓	1000	1000	1000	1000	1000	1000	1000
Warm-up epochs	✓	500	500	500	500	500	500	500
Learning rate	✓	0.00005	0.00001	0.00001	0.00005	0.001	0.00001	0.00001
Feature masking rate ($T_{f,1}$)	✓	0.2	0.2	0.2	0.2	0.2	0.2	0.2
Feature masking rate ($T_{f,2}$)	✓	0.2	0.2	0.2	0.2	0.2	0.2	0.2
Edge masking rate ($T_{e,1}$)	✓	0.2	0.2	0.2	0.2	0.2	0.2	0.2
Edge masking rate ($T_{e,2}$)	✓	0.2	0.2	0.2	0.2	0.2	0.2	0.2

1155 Additionally, we conducted a grid search primarily targeting the learning rate and loss balancing
 1156 parameters for the baseline models. The learning rates for all baselines were explored within the
 1157 search space $\{0.00001, 0.00005, 0.0001, 0.0005, 0.001, 0.005, 0.01, 0.05\}$. Similarly, the loss bal-
 1158 ancancing parameters were tuned across the range $\{0.1, 1.0, 10.0\}$ including their default parameter.
 1159 More precisely, for SEDR, it searched learning rate and balance parameters regarding reconstruc-
 1160 tion loss, VGAE loss, and self-supervised loss. For STAGATE, the search focused solely on the
 1161 learning rate. In the case of SpaCAE, both the learning rate and the spatial expression augmentation
 1162 parameter (α) were tuned within $\{0.5, 1.0\}$. SpaceFlow was optimized by adjusting the learning
 1163 rate and the spatial consistency loss balancing parameter. For GraphST, we explored the learning
 1164 rate and the balancing parameters for feature reconstruction loss and self-supervised contrastive
 1165 loss. Regarding STAligner, we searched for the optimal learning rates for both the pretrained model
 1166 (i.e., STAGATE) and the fine-tuning process. Finally, for scSLAT, we applied the default parame-
 1167 ters since the experiments were conducted under identical settings and with the same dataset. This
 1168 systematic parameter-tuning process facilitated the effective optimization of each baseline model’s
 1169 performance.

1170 E.2 UNSUPERVISED HYPERPARAMETER SEARCH STRATEGY

1171 To apply Spotscape to new data, an appropriate hyperparameter search strategy is essential. Fortu-
 1172 nately, Spotscape is largely robust to hyperparameters, with the exception of the learning rate,
 1173 which is inherently sensitive in gradient-based optimization models. For this reason, we fix all
 1174 parameters except the learning rate and search for the learning rate that maximizes the silhouette
 1175 score, which can be achieved without any supervised information. Specifically, λ_{PCL} , λ_{SS} , and
 1176 τ are set to 0.0005, 10, and 0.75, respectively, while the learning rate is selected from the set
 1177 $\{0.00001, 0.00005, 0.0001, 0.0005, 0.001\}$. Using this hyperparameter optimization strategy, we
 1178 obtained the hyperparameters listed in Table 11 and reported the computed silhouette scores during
 1179 the search process for DLPFC in Figure 21. We then compared the performance of the hyperparam-
 1180 eters optimized without supervision with that of the hyperparameters optimized with supervision,
 1181 which were used solely for performance comparison with the baseline methods in Figure 22. In
 1182 this comparison, the performances of both sets of hyperparameters are competitive, with the unsu-
 1183 pervised optimization showing even better performance in some cases, thereby demonstrating the
 1184 effectiveness of our search strategy and confirming the robustness of hyperparameter sensitivity.

1188

1189

1190

1191

1192

1193

1194

1195

1196

1197

1198

1199

1200

1201

1202

1203

1204

1205

1206

1207

1208

1209

1210

1211

1212

1213

1214

1215

1216

1217

1218

1219

1220

1221

1222

1223

1224

1225

1226

1227

1228

1229

1230

1231

1232

Table 11: Optimized hyperparameter settings for Spotscape

Type	Dataset	λ_{PCL}	λ_{SS}	τ	Learning Rate
Single	DLPFC Patient 1	0.0005	-	0.75	0.00005
Single	DLPFC Patient 2	0.0005	-	0.75	0.0001
Single	DLPFC Patient 3	0.0005	-	0.75	0.0001
Single	MTG Control	0.0005	-	0.75	0.0005
Single	MTG AD	0.0005	-	0.75	0.0001
Single	Mouse Embryo	0.0005	-	0.75	0.0001
Single	NSCLC	0.0005	-	0.75	0.0001
Multi Integration	DLPFC	0.0005	10	0.75	0.0005
Multi Integration	MTG	0.0005	10	0.75	0.001
Multi Alignment	Mouse Embryo	0.0005	10	0.75	0.0005
Multi Alignment	Breast Cancer	0.0005	10	0.75	0.0005

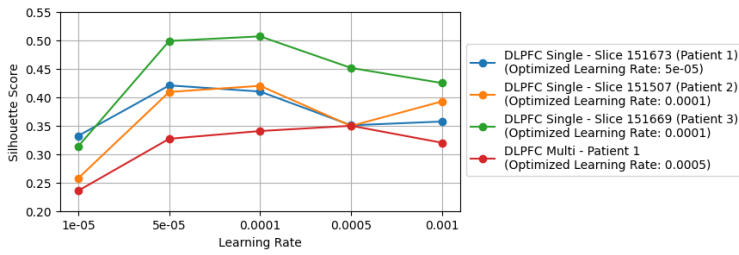


Figure 21: Unsupervised hyperparameter searching strategy using silhouette scores.

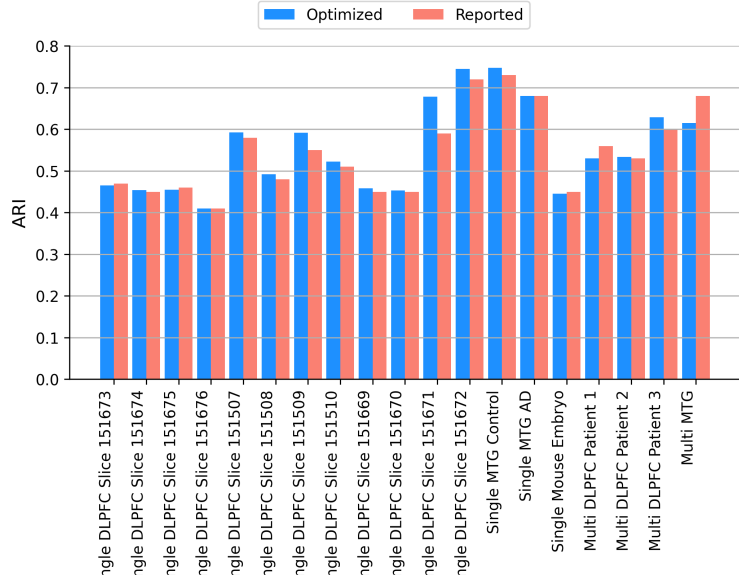


Figure 22: Performance comparison between optimized and reported hyperparameters.

E.3 IMPLEMENTATION DETAILS

Model architecture and training. The model employs a 2-layer GCN (Kipf & Welling, 2016) as the GNN-based encoder and a 2-layer MLP as the decoder, both utilizing batch normalization and ReLU activation functions. The encoder’s hidden dimensions are set to $[N_g, 256, 64]$, while the decoder’s dimensions are configured as $[64, 256, N_g]$. The clustering process in PCL is performed $T = 3$ times, with the K -means granularity set to $[K, 1.5K, 2K]$ to get a fine-grained representation. Optimization is carried out using the Adam optimizer with a learning rate determined through hyperparameter searching (see Appendix E.1) and a weight decay of 0.0001. All experiments are repeated 10 times, and we report the mean and standard deviation for each performance metric.

Preprocessing. We follow the preprocessing methodology described in prior work (Dong & Zhang, 2022). Initially, 5000 highly variable genes are selected using Seurat v3 (Stuart et al., 2019). The

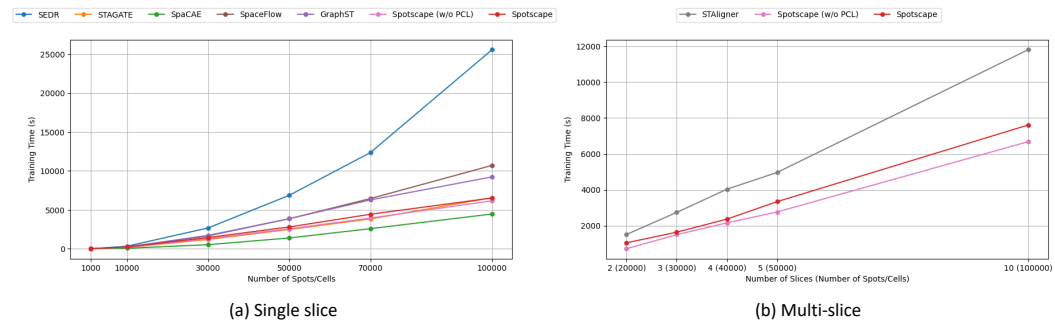
1242 data is then normalized to a CPM target of 10,000 and log-transformed using the SCANPY package
 1243 (Wolf et al., 2018a). For datasets with multiple slices, we concatenate the slices to enable integration
 1244 or alignment.

1245 **Computational Resources.** All the experiments are conducted on Intel Xeon Gold 6326 CPU and
 1246 NVIDIA GeForce A6000 (48GB).

1247 **Software Configuration.** Spotscape is implemented in Python 3 (version 3.9.7) using Py-
 1248 Torch 2.1.1 (<https://pytorch.org/>) with Pytorch Geometric (https://github.com/pyg-team/pytorch_geometric) packages.
 1250

1252 F SCALABILITY OF SPOTSCAPE

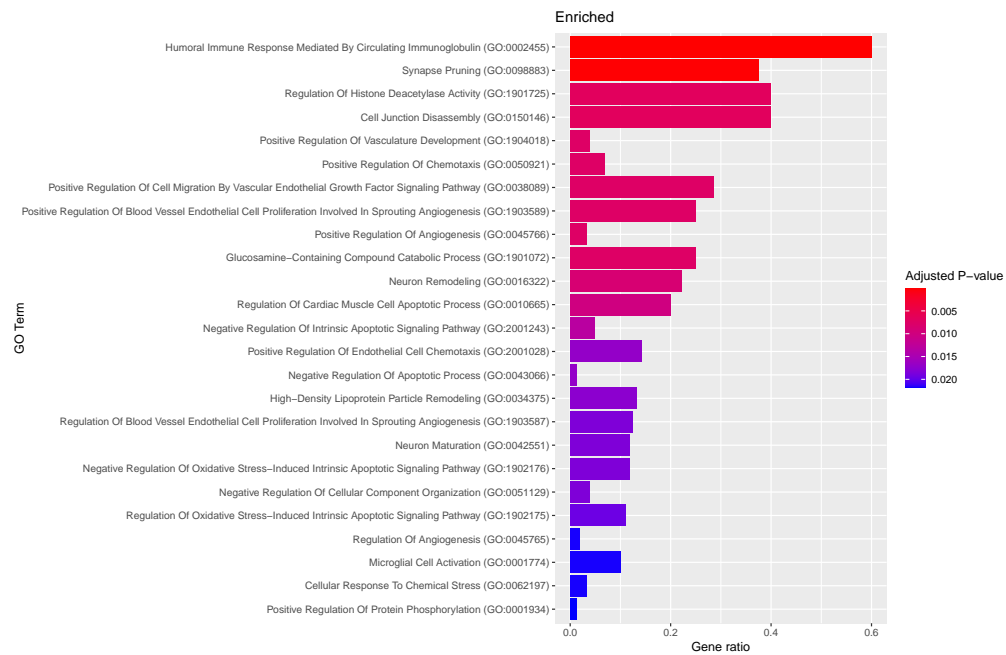
1254 Due to recent advancements in high-throughput sequencing machines, the scalability of models has
 1255 become a critical factor in validating their performance. To this end, we generate a synthesized
 1256 dataset by downsampling or oversampling the Mouse Embryo dataset to create data with 1,000 to
 1257 100,000 spots, and report the running time in Figure 23. We observed that Spotscape requires
 1258 relatively more training time than baseline methods due to the prototypical contrastive learning
 1259 objective. However, the training time of Spotscape scales linearly with the number of spots, rather
 1260 than quadratically or exponentially. This linear scalability ensures that SpotScape remains practical
 1261 for high-throughput datasets (e.g., 100,000 spots) within a reasonable timeframe. Moreover, we
 1262 would like to emphasize that Spotscape without the prototypical learning scheme exhibits faster
 1263 running times. Thus, if fast inference is required, this option can be used, albeit with a trade-off in
 1264 performance.



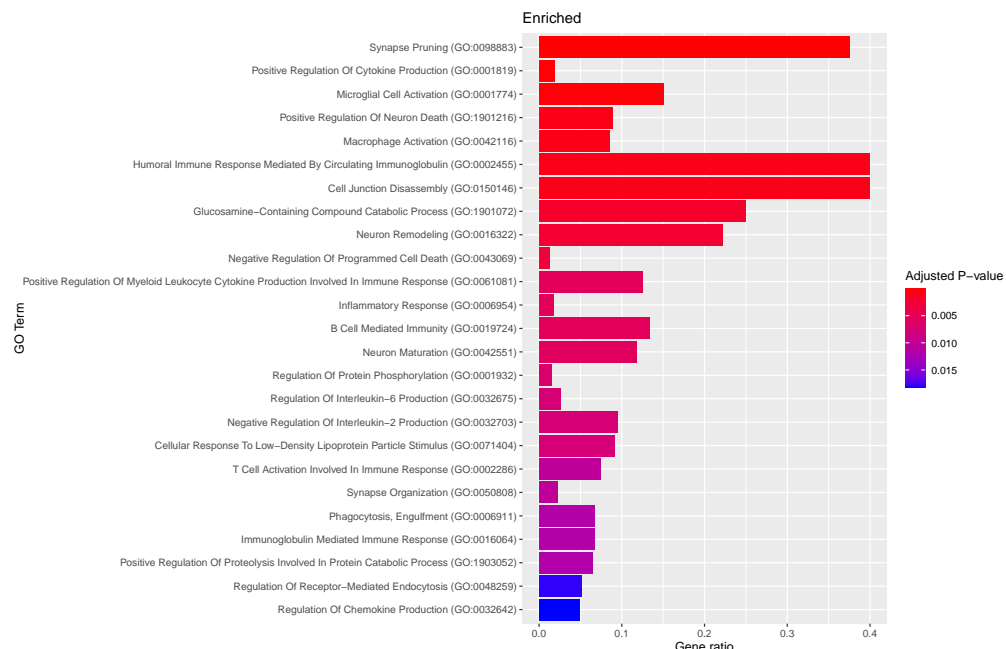
1274 Figure 23: The running time of Spotscape and baseline methods over the various number of spots
 1275 on (a) the single and (b) multi-slice dataset.
 1277

1296 **G DIFFERENTIALLY EXPRESSED GENE ANALYSIS**
 1297

1298 Genes with $\log_2(\text{fold}) > 0.25$ and adjusted p-value from DESeq2, implemented in FindMarkers
 1299 from Seurat V4 (Hao et al., 2023) < 0.05 are determined as DEGs.
 1300



1322 Figure 24: Differential gene analysis and gene ontology enrichment analysis for biological process
 1323 between AD and PSP in cluster 6 (layer 2).
 1324



1346 Figure 25: Differential gene analysis and gene ontology enrichment analysis for biological process
 1347 between AD and PSP in cluster 4 (layer 5).
 1348

1349

1350 H TRAJECTORY ANALYSIS

1351
 1352 We perform trajectory inference tasks to evaluate whether the representation learned by
 1353 Spotscape effectively captures underlying trajectories in spatial transcriptomic data. For quan-
 1354 titative validation, we assign numerical values to layers as follows: WM = 0, layer 6 = 1, layer 5 = 2,
 1355 layer 4 = 3, layer 3 = 4, layer 2 = 5, and layer 1 = 6. We then calculate pseudo-Spatiotemporal Map
 1356 (pSM) values following the approach described in SpaceFlow Ren et al. (2022) using the represen-
 1357 tation from each model. Finally, we compute the correlation between these assigned values and the
 1358 calculated pSM values and report the results in Figure 26. In these results, Spotscape demonstrates
 1359 effectiveness in the trajectory inference task, further validating its broad applicability. Additionally,
 1360 it is worth noting that while Spotscape employs a prototypical contrastive learning scheme that
 1361 could make the latent space discrete, potentially negatively affecting the trajectory inference task,
 1362 Spotscape is not dominated by this module and still demonstrates strong performance as long as
 1363 the balance coefficient (L_{Pro}) is not set too high. We also present these results visually in Figure 27.

1364

1365

1366

1367

1368

1369

1370

1371

1372

1373

1374

1375

1376

1377

1378

1379

1380

1381

1382

1383

1384

1385

1386

1387

1388

1389

1390

1391

1392

1393

1394

1395

1396

1397

1398

1399

1400

1401

1402

1403

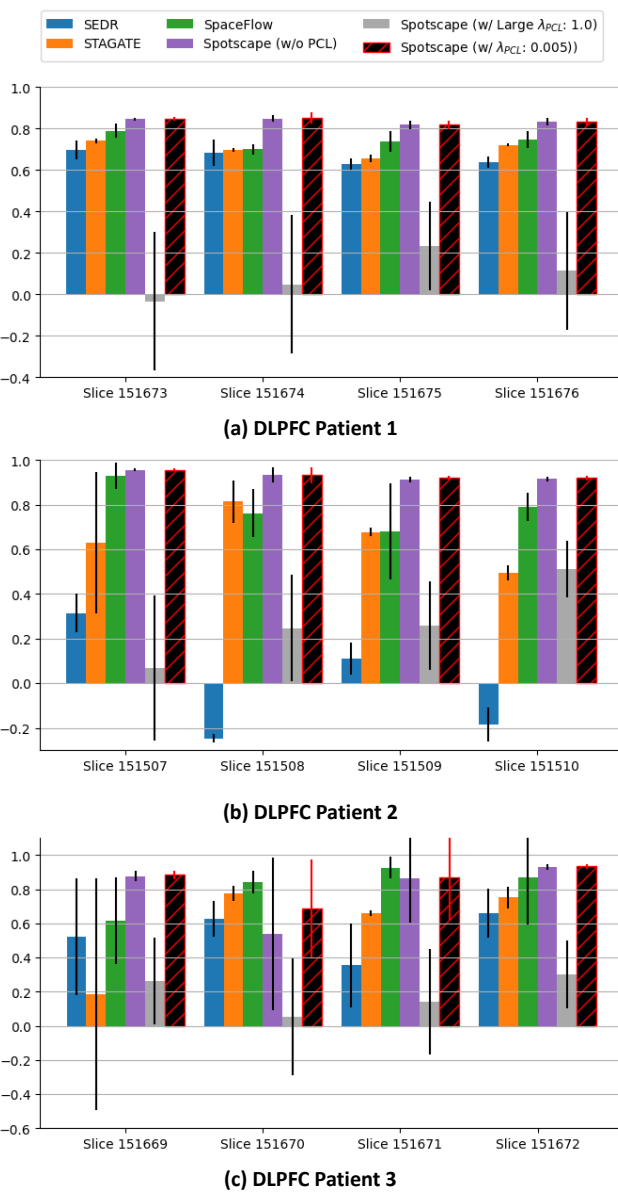


Figure 26: Correlation Coefficient between pseudo-Spatiotemporal Map and Layers in DLPFC.

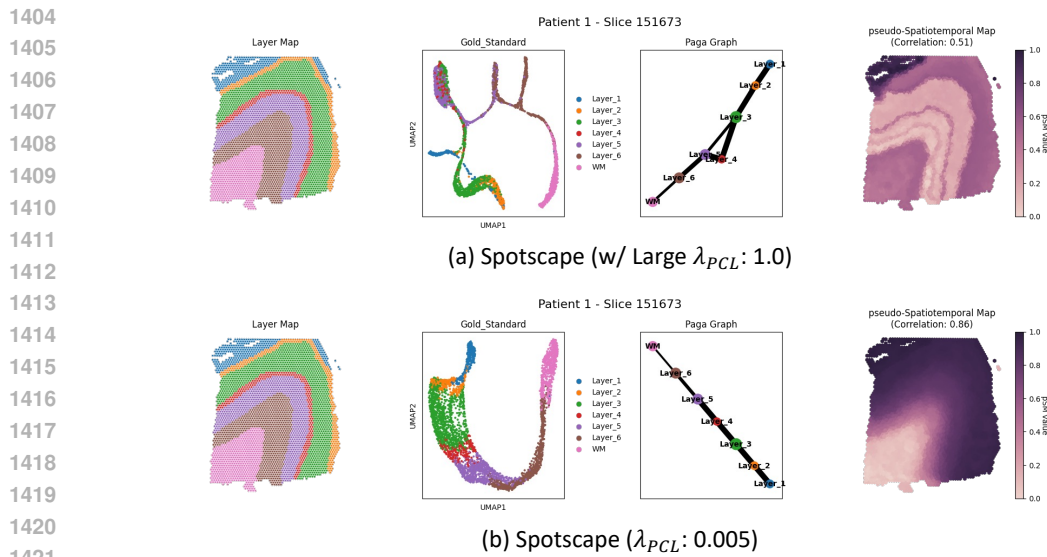


Figure 27: Trajectory inference results of Spotscape.

I IMPUTATION

To demonstrate the additional benefits of incorporating a decoder layer and reconstruction loss, we performed imputation tasks to highlight the effectiveness of our reconstructed output in imputing missing values and denoising noise present in the raw data. In the experiment shown in Figure 28, we masked certain non-zero values in the data and evaluated whether the model successfully recovers these values, following the settings from previous works Lee et al. (2024). From these results, Spotscape outperforms in terms of both RMSE and median L1-distance, demonstrating its superiority in imputation tasks. Moreover, we also examine whether the imputed outputs can help identify marker genes that were not differently expressed in the raw data, illustrated in Figure 29. We conduct these experiments for the known marker genes in the brain cortex layer. Specifically, RORB serves as a canonical marker for layer 4 neurons (Clark et al., 2020); ETV1 is associated with layer 5 neurons (Goralski et al., 2024); NTNG2 and NR4A2 are well-recognized markers for layer 6 neurons (Maynard et al., 2021; Darbandi et al., 2018); and OLIG2 is indicative of white matter regions (Wegener et al., 2015). The results show that after imputation using Spotscape, marker genes are more distinctly expressed, demonstrating the practical applicability of Spotscape.

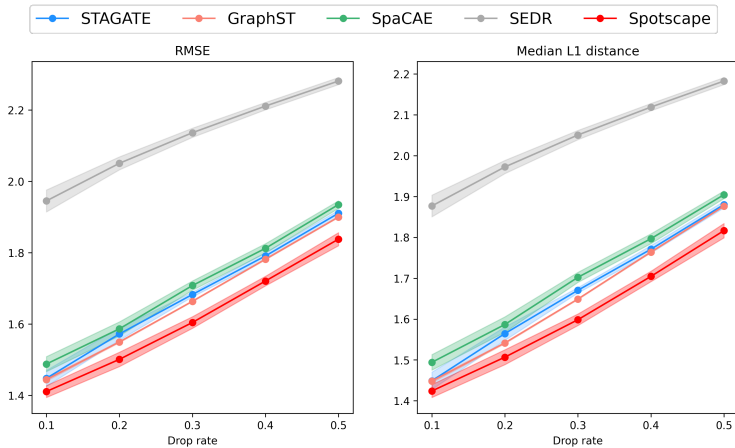


Figure 28: Imputation error comparison across various drop rates in the DLPFC.

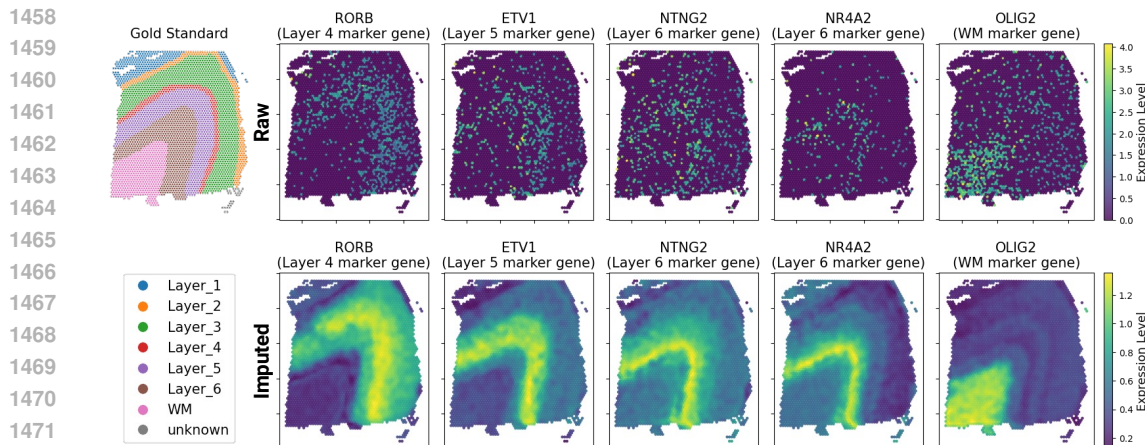


Figure 29: Spatial expression of raw and Spotscape imputed data for marker genes in the DLPFC.

J FUTURE WORKS

In this work, we discover that reflecting the global relationships between spots provides significant information on SRT data; however, we currently leverage this relationship only implicitly through the loss function. We recognize that the model could benefit from incorporating more complex interactions by constructing edges between spots, thereby implementing graph structure learning. Future work could explore this avenue to enhance the representation of spatial relationships, allowing the model to leverage valuable information from the global context more effectively.

Furthermore, SRT data frequently includes histology images that offer critical contextual information about tissue architecture and cellular organization. However, in this study, we concentrate on a more general case that limits our analysis to spatial coordinates and gene expression profiles, potentially overlooking the rich insights that histological features could provide. We anticipate that integrating this information with Spotscape could represent a promising direction for future research.